Magnetic Fields in High Velocity Clouds and Rotation Measure Foreground Removal Techniques

Olivia Walters

Supervisors: Craig Anderson, Naomi McClure-Griffiths

An honours thesis submitted for

The Australian National University
Research School of Astronomy and Astrophysics

October 2024

Except where otherwise indicated, this thesis is my own original work.

Olivia Walters
23 October 2024

Acknowledgments

I would like to thank my primary and secondary supervisors, Dr. Craig Anderson and Prof. Naomi-McClure Griffiths for being the main body of support, data, and ideas when writing this thesis. I would also like to acknowledge Prof. Bryan Gaensler and Dr. Lyla Jung for providing further aid in the process of analysis, and their support in regards to POSSUM itself. The ASKAP POSSUM team more broadly has come as a great aid and source of community during the production of this thesis.

Fellow radio astronomer Callum Lynn has also been a great source of advice and help in constructing this thesis for a more general astronomical audience, along with his guidance about the honours and PhD process.

The ANU SSN Consultancy Group was a crucial part in the validation of the statistical techniques listed in this paper, including the suggestion to use the Weighted ANOVA and Tukey HSD test.

I would also like to thank my grandmother, Hilda Filipovic, for being a very important person in my life, and a rock on which I relied on in the process of completeing my honours year.

Abstract

Context. High Velocity Clouds (HVCs) are a proposed solution to how extragalactic gas enters into star-forming galaxies. However, the presence of enveloping magnetic fields is required to ensure that HVCs can travel through the halo without being torn apart by ram pressure. This hypothesis, in the context of HVCs, is referred to as 'magnetic draping'.

Aims. This report aims to detect the signature of magnetic draping in HVCs and evaluate the strength of magnetic fields enveloping HVCs - both using a newly constructed rudimentary algorithm applicable to a broad range of HVCs. A secondary goal of the report is on the investigation of image processing of interpolated data to solve anticipated resolution issues with higher-quality SKA-era interpolated rotation measure data.

Data. Recent rotation measure data was retrieved in May 2024 from the Polarisation Sky Survey of the Universe's Magnetism (POSSUM) and HVC data was retrieved the Galactic All Sky Survey (GASS). An interpolation of legacy rotation measure data was retrieved from the Galactic Faraday rotation sky 2020.

Methods. The Kolmogorov-Smirnov test assuming a spherical HVC morphology was used to detect magnetic draping by determining the difference between in-HVC and out-HVC rotation measure populations. Two new statistical methods to evaluate the magnitude of magnetic draping were proposed, in addition to the use of a previous method sanctioned by literature. Several image processing techniques, including Fourier analysis, were visually and statistically analysed as to their efficacy at removing objects of a particular angular scale.

Results. Of 13 HVCs analysed, a magnetic field signature of 11 HVCs was found to within 99.9% confidence. One of the proposed methods, called 'variance subtraction' displayed statistical agreement with the traditional weighted mean method. The average HVC magnetic field is an order of magnitude greater than or equal to than in simulations, at scales of 1 μG. A two-dimensional bandpass method was found to be adequate at correcting identified problems with interpolated data, witout loss of validity.

Contents

List of Figures

Honours Thesis – 23 October 2024

List of Tables

Introduction

The question of how gas is accreted into galaxies, fuelling star-formation, is a puzzle that has perplexed astronomers for decades [Lockman et al., 2008; Grønnow et al., 2017]. Due to the complexities in the structures of star-forming galaxies, there are many factors involved in the process of, and potential sources of accretion. What astronomers do know, at least, is that star-forming galaxies require a continuous supply of fresh gas to continue their star formation [Lockman et al., 2008; Grønnow et al., 2017; Putman et al., 2012].

Due to observational constraints, astronomers attempt to answer this question by examining the behaviours of our own Milky Way and Local Group environment, assuming the Milky Way is typical of a star-forming galaxy.

A major factor to consider when answering this question is where fresh pristine gas comes from, and by what mechanism it takes to enter the disks of star-forming galaxies [Wakker and van Woerden, 1997; Lockman et al., 2008; Hill et al., 2009]. High Velocity Clouds (HVCs) have been a suggested mechanism for Galactic gas accretion and this report aims to evaluate the viability of this suggestion [Moss et al., 2013; Putman et al., 2012].

1.1   High Velocity Clouds

HVCs are clouds of gas found in the Milky Way's Circumgalactic Medium (CGM) and Galactic halo. They have a high peculiar velocity relative to the Galactic Standard of Rest (GSR), typically 70-90 kms^{-1} [Wakker, 1991; Wakker and van Woerden, 1997]. As will be shown in section 1.2.1, this increased speed, and its interaction with halo magnetic fields, is hypothesized to allow the HVC to survive as it travels through the CGM and halo so it can reach the Galactic disk and Interstellar Medium (ISM) of the Milky Way.

There are a few hypothesises as to where HVCs originate. Putman et al. [2012] suggests that HVCs originate from the Intergalactic Medium (IGM) surrounding the local group. However, there is also a belief that some HVCs likely 'tore off' from satellites like the Magellanic Clouds, due to the presence of their own dark matter subhaloes, and the existence of HVCs in the Magellanic Stream and Leading Arm [Kaczmarek et al., 2017; McClure-Griffiths et al., 2010]. Recent simulations from TNG50 have in-

Figure 1.1: From Konz et al. [2002], figure 2. An example of a typical HVC shape and structure, specifically that of HVC125+41-207. The contour lines and shading indicate HI column density.

dicated that HVCs mainly have their origins in the warm-hot CGM, formed through cooling from thermal instabilities [Lucchini et al., 2024].

HVCs typically have a neutral mass gas content of $10^5 - 3 \times 10^5 M_\odot$ [Putman et al., 2012]. They are generally shaped like comets, with a primary bulb that is approximately 0.5-15 kpc in diameter - a value that is highly dependent on distance to the Galactic midplane, which can range from approx. 2 - 25 kpc [Putman et al., 2012; Konz et al., 2002]. Furthermore, HVCs have tail-like structures that account for one eighth the baryonic mass of the HVC [Konz et al., 2002]. These tails leave behind long streams of gas that remain after collision with the Galactic disk [Putman et al., 2012]. This size-distance correlation, comet-like structure, and long streaming tails suggest quite conclusively that HVCs shed large quantities of material as they make their journey to the ISM.

Figure 1.1 is from Konz et al. [2002], which provides a typical example of what a HVC looks like in HI, specifically using the example of HVC125+41-207.

1.2   Magnetic Fields

The primary issue facing HVCs as an explanation for gas accretion is its capacity to remain whole as it travels through the CGM and Galactic halo. As discussed, in section 1.1, HVCs can loose a lot of size and mass as it approaches the Galactic disk, with the long trails it leaves behind being evidence for ram-pressure stripping as the HVC collides with the gas present in the halo [Jones et al., 1996; Grønnow et al., 2017, 2022]. Heitsch and Putman [2009] demonstrates that without anything to counter this effect, HVCs with masses under $10^{4.5} M_\odot$ would completely disperse within 10 kpc of halo travel.

Additionally, HVCs are subject to Kelvin-Helmholtz (K-H) instabilities, which is triggered by the nature of the HVC being a cloud of cold gas travelling at high speeds through a medium of hot halo gas. These K-H instabilities are a significant factor that would lead a to HVC dispersal before reaching the Galactic disk [Jones et al., 1996; Grønnow et al., 2017, 2022].

1.2.1 Draping

The proposed solution to handle this problem is magnetic fields. The Galactic halo is magnetised to some degree [Mao et al., 2010; Han and Qiao, 1994; Jung et al., 2023; Beck et al., 2012]. It is hypothesised that HVCs accumulate these existing magnetic fields in the Galactic halo, causing them to cloak the HVC with a shield that protects against ram pressure stripping and supresses K-H instabilities [Dursi and Pfrommer, 2008; Jones et al., 1996; Konz et al., 2002; Grønnow et al., 2017, 2018; Jung et al., 2022]. This phenomenon is referred to as 'magnetic draping'.

There is not enough observational evidence to support the magnetic draping hypothesis. However, with recent advancements in: RM radio surveys [Gaensler et al., 2010, 2024; Vanderwoude et al., 2024; Moss et al., 2013; Westmeier, 2018; Taylor et al., 2009; Finkbeiner, 2003; Hutschenreuter and Enßlin, 2020; Hutschenreuter et al., 2022]; the analysis of ram pressure stripping [Jones et al., 1996; Grønnow et al., 2017, 2022]; measurement and estimation of magnetic fields [Betti et al., 2019; Grønnow et al., 2017; Mao et al., 2010; Jones et al., 1996; Hill et al., 2013; Schnitzeler, 2010]; and simulations of HVCs [Konz et al., 2002; Grønnow et al., 2017, 2018, 2022; Jung et al., 2022] – it is now possible to attempt to observe and analyse the role of magnetic draping in HVCs observationally.

Previous and recent simulations involve reports produced by Grønnow et al. [2017, 2018, 2022] (henceforth referred to as the "Grønnow et al. simulations") that provide detailed insight onto how a magnetic draping protects HVCs from collapse, complementing earlier work by Konz et al. [2002]; Jones et al. [1996]. It is shown from the Grønnow et al. simulations that magnetic fields of about 0.3-1 μG can provide stability to HVCs.

However, increasing magnetic field strength beyond a certain threshold can result in less stability; magnetic fields can accelerate the effects of Rayleigh-Taylor (R-T) instabilities and the magnetic pressure applied by the draped fields can also slow down a HVC to the point that it no longer is fast enough to sweep up these magnetic fields. From the Grønnow et al. simulations, the upper threshold where these effects start increasing instability is on the order of 1 μG (specifically stating a maximum of approx. 3 μG), thus HVCs should ideally have a "Goldilocks" magnetic field strength on the order of magnitude of 0.1μG, with 1μG being too high, and 0.01μG being too low.

The effectiveness of magnetic draping is affected by the morphology of these fields

and the physical properties of the HVC. The Grønnow et al. simulations state that both the orientation of the magnetic field with respect to the direction of motion of the HVC, and where the magnetic field is located are important considerations. It is expected that the HVC is not entirely covered in a magnetic field, only the part that is front facing in the direction of travel. While it is possible to draw conclusions about the survivability of a HVC from the strength of the magnetic field, modelling is required to confirm the accuracy of such conclusions [Betti et al., 2019]. The Grønnow et al. simulations also predict that metallicity can affect the HVC's survivability, via affecting phase transitions, with high-density metal-rich clouds and low-density metal-poor clouds being more unstable than HVCs of the opposite compositions.

The simulations by Jung et al. [2022] predict higher magnetic field strengths on the order of 1 µG. It is very clear that even simulationaly, the specific strengths of magnetic fields surrounding HVCs have high uncertainty. The results of this report will still compare against the Grønnow et al. simulations despite this.

1.2.2 Faraday Rotation

Magnetic fields cannot directly be imaged by a telescope. Instead, researchers can use the phenomenon of Faraday Rotation to quantify the line-of-sight magnetic field strength. Polarised radiation tends to rotate as it travels through a medium with a magnetic field present. This effect is quantified by equation 1.1.

$$\Delta\psi = \phi\lambda^2 \tag{1.1}$$

Where λ is the wavelength of radiation, ϕ is the faraday depth and $\Delta\psi$ is the change in polarisation angle. Thus, by recording the stokes parameters of incoming light from distant radio sources, one can derive the Rotation Measure (RM) of incoming radiation, which is a statistical quantifier of Faraday Rotation and faraday depth [Vanderwoude et al., 2024; Brentjens and de Bruyn, 2005]. For the purposes of this report, rotation measure and faraday depth are treated as equivalent henceforth, despite their subtle differences.

For illustrative purposes, a schematic diagram of how Faraday Rotation is measured by telescopes on Earth with the aim of analysing HVCs are shown in figure 1.4.

Vanderwoude et al. [2024] describes the method by which this report's main source, the Polarisation Sky Survey of the Universe's Magnetism (POSSUM), obtained its RMs from radio observations. There is a direct connection between RM and line-of-sight magnetic field strength, quantified by equation 1.2 [Betti et al., 2019; Vanderwoude et al., 2024; Hill et al., 2013; Kaczmarek et al., 2017; Mao et al., 2010].

$$RM = 0.812 \int_{s_{\text{observer}}}^{s_{\text{source}}} \frac{n_e(s)}{\text{cm}^{-2}} \frac{B_\parallel}{\mu G} \frac{ds}{\text{pc}} \text{rad m}^{-2} \tag{1.2}$$
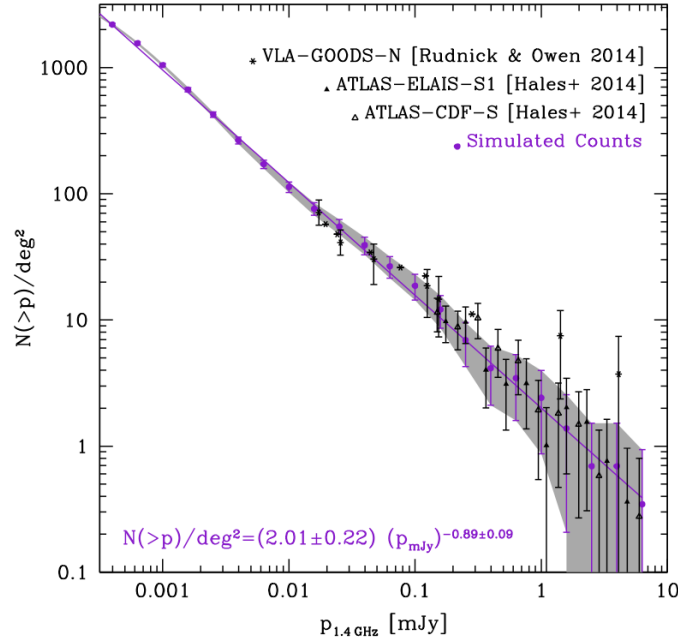
Figure 1.2: From Loi et al. [2019], figure 4. A graph of the relationship between the sensitivity at 1.4 GHz (x-axis) and the average mimumum number of RM sample points per square degree (y-axis). The black points are not relevant to the report, but the purple line and equation describe the determined relationship.

In which, $B_\parallel$ is the line-of-sight magnetic field strength, RM is the Rotation Measure, and n_e is the electron density of the medium as a function of line-of-sight distance s. The analysis of this equation, its solutions, and the use of it in calculating the magnitude of line-of-sight magnetic fields is discussed in section 4.

Faraday Rotation also occurs in the ISM of the Milky Way, due to the slight magnetisation of the ISM [Ferrière, 2001; Mao et al., 2010; Schnitzeler, 2010]. This magnetisation is antisymmetric with galactic longnitude [Mao et al., 2010]. Hence it is also important to remove the foreground from RM observations.

When making radio observations of RMs, a principal factor to consider is the observational signal to noise ratio and detector sensitivity. Radio sources tend to appear in the field after high exposure times as point-like sources. These point-like sources are then collated into an "RM grid" which has a particular density measured in sample points per square degree. The sensitivity of a detector and total integration time determines the number of source points observed as seen in figure 1.2 [Loi et al., 2019].

Signal to noise is of primary concern when measuring the effect of Faraday Rotation. At low enough signal-to-noise ratios, it is possible to encounter noise peaks which do not accurately represent the real RM [Macquart et al., 2012]. Figure 1.3 gives

a visual illustration of this phenomenon. The issue in question is that any observation of RM grids is going to dip below the signal-to-noise threshold of approx. 6, which can introduce an intrinsic scatter in collected RM grid data. Thus RM points below this threshold are ignored. However, the dataset masks out all RMs below a signal to noise of 8, which is considered conservative [Gaensler et al., 2024].

As will be discussed in section 2.1, the POSSUM dataset is the first dataset with 30 RMs per square degree versus legacy surveys which had only 1 RM per square degree.

1.3 Temperature, Chemical Properites, and Emission

Due to their hypothesised origins in extragalactic gas, HVCs contain mostly hydrogen gas such as HI, which can be seen with 21 cm emission [Wakker, 1991; Wakker and van Woerden, 1997; Westmeier, 2018]. The proportion of ionised gas in HVCs is still heavily debated. HVCs also emit H-alpha, however due to extinction effects, it is difficult to observe [Bland-Hawthorn and Maloney, 1999; Finkbeiner, 2003].

HVCs have a temperature relationship with proximity to the Galactic midplane, with an average HVC temperature of 10000 K and a range of temperatures ranging from 8000 − 12000 K [Hill et al., 2009; Madsen et al., 2006]. The temperature of a HVC is in the region in which atomic hydrogen transitions from neutral (HI) to ionised (HII), suggesting that HVCs may be partly ionised [Hill et al., 2009; Madsen et al., 2006; Kawaguchi, 1952]. This temperature relationship is dependent on their position with respect to the Galactic midplane, with HVCs closer to the midplane generally being cooler [Madsen et al., 2006]. This temperature is contrasted by the Galactic halo temperature, which varies from $\approx 10^4 - 10^6$ K [Putman et al., 2012]. This is an important factor in creating K-H instabilities.

There is evidence that HVCs can contain alpha group elements. Hill et al. [2009]; Madsen et al. [2006] found the presence of [NII] 6583Å, [SII] 6716Å, and [OIII] 5007Å emission lines – with a conclusion that Nitrogen abundance is 0.15-0.44 times solar abundance levels. The observation of these emission lines can help constrain the metallicity of any HVC [Hill et al., 2009]. Metallicity is important in both how HVCs act as fresh gas supplies for star formation, as well as the mechanism by which HVCs can survive their transit through the CGM [Grønnow et al., 2018]. While HVCs can contain heavier elements Hayakawa and Fukui [2024] finds that these concentrations are low enough that HVCs can remain as viable candidates for fuelling star formation via gas accretion.
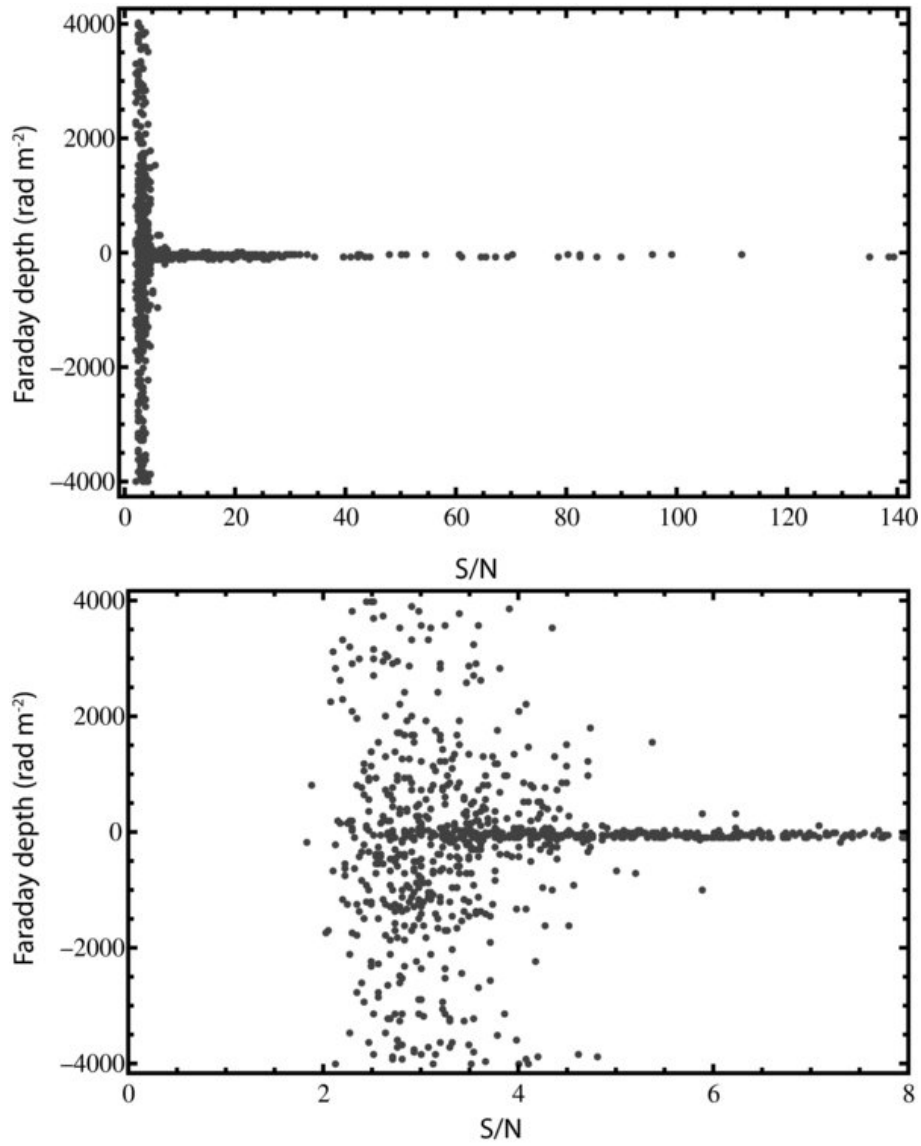
Figure 1.3: From Macquart et al. [2012], figure 1. A graph displaying the effect of observational (stokes parameters) signal-to-noise ratio the resultant faraday depth on a sample set of observations.
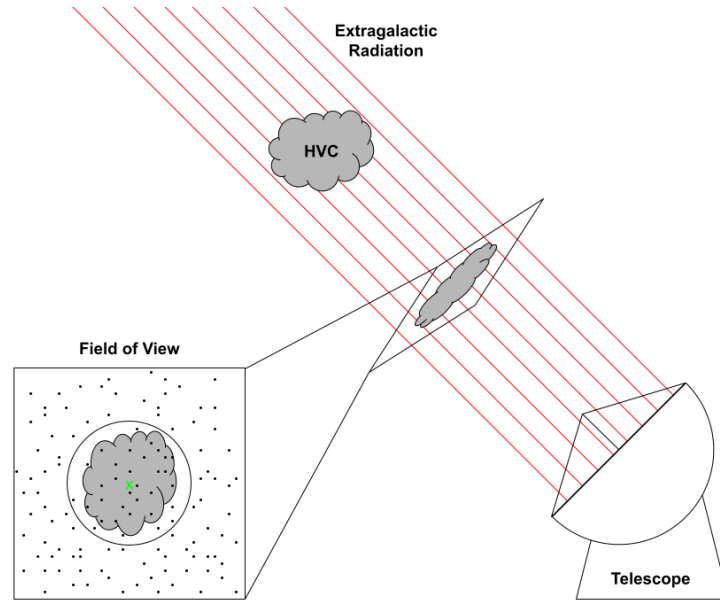
Figure 1.4: An schematic diagram illustrating how the RM of incoming radio radiation is observed, notably around HVCs. Note that the extragalactic radiation will appear as randomly distributed across the field of view.

1.4   Smith Cloud

While previous surveys have lacked the capacity to observe magnetic fields surrounding HVCs, the Smith Cloud is an exception to this rule due to its size and proximity to the Milky Way ISM.

The Smith Cloud is a large HVC that is in the process of colliding with the Galactic disk [Lockman et al., 2008; Tepper-García and Bland-Hawthorn, 2017; Lockman, 2008]. Unlike most HVCs it is quite large in both mass (at least $10^6 M_\odot$ in HI mass) and angular size (the main bulb covering an area of approx. 144 square degrees) [Lockman et al., 2008; Tepper-García and Bland-Hawthorn, 2017; Lockman, 2008]. It has a predicted physical size of 3 square kpc, which is large for a HVC close to the Galactic disk [Lockman et al., 2008]. Due to its proximity and size, the Smith Cloud has been used as a source point of analysis for most of the properties already discussed. For example, metallicity tracers and alpha-group elements in Madsen et al. [2006]; Hill et al. [2009] were determined by analysing the Smith Cloud. The figure from Lockman et al. [2008] appears in appendix as figure 1.5.

Simulations by Grønnow et al. [2017] and observations by Hill et al. [2013] both agree on an effective magnetic field of ∼8 µG. Note that this number is well above the Goldilocks zone mentioned in section 1.2.1 – indicating the potential exceptionality of the Smith Cloud.
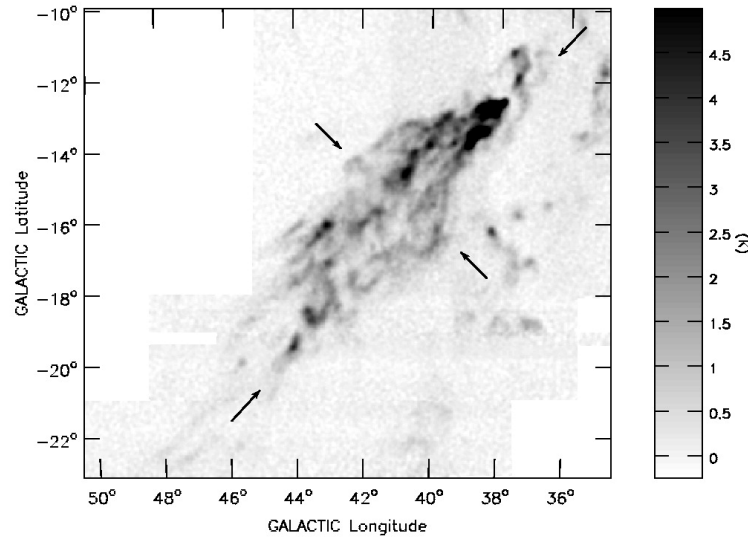
Figure 1.5: From Lockman et al. [2008], figure 1. A HI image of the Smith Cloud taken from the Green Bank Telescope at a local standard of velocity rest of 100 kms^{-1}. The purpose of the arrows are not meaningful to this paper.

While there are other HVCs that have been sampled in the past, the Smith Cloud has been the main source of HVC information. This is a problem, as the Smith Cloud is an outlier amongst most HVCs – evidenced by its unusual size and magnetic field strength - compared to predictions - both factors being related. There is a necessity to analyse more typical nearby HVCs to gain an understanding of the effects of magnetic fields.

1.5   Report Outline and Objectives

The primary objective of this report is to (a) construct a rudimentary algorithm for evaluating the prescence of detectable magnetic field profies in HVCs found in the CGM and halo and, (b) use this base algorithm to come up with a *very* rough estimate for the magnetic field strength surrounding typical HVCs. The primary source of data will be POSSUM, with its newfound grid densities allowing for the fullfilment of the primary objective. Despite this, there is a lack of ability to measure magnetic fields to decent prescision. This mandates a set of required assumptions to allow for an initial estimate of the field strength for any HVC. The best-case scenario is an estimate that is accurate within a single order of magnitude. Hence, why the aim of this report is to lay the foundations for a future, more detailed analysis, of numerous HVCs (up to 1693 objects as discussed in section 2.3).

There is a secondary objective that is integral to completing the primary objective: that of foreground removal. Past research, specifically within the analysis of HVCs,

has relied on the interpolation of legacy RM grid data to obtain a RM foreground to use in corrections [Schnitzeler, 2010; Hill et al., 2013]. However, as researchers move onto measurements of RM that demand more accuracy, foreground removal needs to equally match that growing need for accuracy – thus this report also aims to investigate avenues for improving foreground subtraction techniques.

This report is split into six sections plus an appendix. Section 2 describes the process of how and which data was obtained to achieve the research question, and how this data was collated. Section 3 summarises the investigation into foreground removal, which is the secondary aim of the research. Section 4 describes how the magnetic fields for HVCs were detected and derived. Section 5 discusses the viability of the methods described in the report, along with broader scientific and statistical considerations. Lastly, section 6 concludes and outlines the many possible directions for future research. Appendix A lists information on how to obtain the program data and algorithms used in research.

Data

To achieve the goals listed in section 1.5 - namely to detect and measure the magnetic field profiles of HVCs and improve RM foreground removal techniques - several sources of data are required including RM grid data, interpolations, and HVC catalogs. Furthermore, work needs to be done to collate the data.

2.1 Faraday Rotation Measures

The Australian Square Kilometre Array Pathfinder (ASKAP) represents a recent development in the progress of the field of radio astronomy. It is a part of a new generation of southern-hemisphere telescopes building towards the Square Kilometre Array (SKA), as provided by Hotan et al. [2021]; Gaensler et al. [2010, 2024].

POSSUM is an ongoing project using ASKAP with a key aim of measuring the RM southern sky. The benefit of using ASKAP as opposed to previous RM sky surveys is the RM grid density ASKAP can provide. Previous surveys such as the NRAO VLA Sky Survey (NVSS) were only able to record an RM grid density of 1 sampling point per square degree, with POSSUM providing a density 30 times greater. The higher grid density allows for the analysis of regular-sized HVCs in the CGM, as opposed to only the largest HVCs like the Smith Cloud.

POSSUM is set to cover a region of the southern sky that has seldom been recorded properly in previous RM grid surveys, primarily due to the lack of RM radio astronomy in the southern sky [Hutschenreuter and Enßlin, 2020; Hutschenreuter et al., 2022; Gaensler et al., 2010, 2024]. This allows for the analysis of HVCs which otherwise would not be analysed under legacy data.

POSSUM data is mostly recorded using the ASKAP radio frequency band 1 at 880-1088 MHz. The POSSUM grid data used in this report represents all collected and processed RMs by the POSSUM survey as of May 2024, with a total RM source count of 188842. Figure 2.1 represents the entire sample on an Aitoff projection.
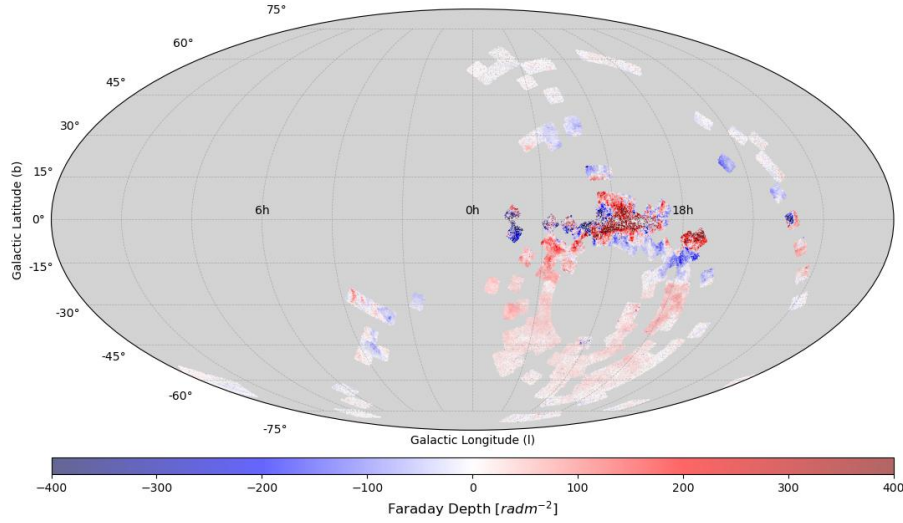
Figure 2.1: An Aitoff projection of all portions of the RM sky observed by ASKAP for the POSSUM survey. The map is up to date as of May 2024 and all RMs in this map are used in the production of this report. The value of these RMs are indicated by colour.

2.2   Ancillary Data

2.2.1   The Galactic Faraday Rotation Sky 2020

The process of estimating RM foreground contributions typically requires the use of of an interpolation between RM grid point measurements. More modern research has been done in interpolating the POSSUM data set, for example the recent paper by Khadir et al. [2024]. However, due to POSSUM's lack of complete sky coverage, it was determined as better to use a whole-sky RM interpolation of legacy data - as a complete interpolation is needed for image processing analysis and the need to rely on more well-used data. The most recent RM sky interpolation came from Hutschenreuter and Enßlin [2020]; Hutschenreuter et al. [2022], which combined all previous sources of RM grid data with free-free emission from the Planck survey. This RM sky reconstruction will be refered to as the "Hutschenreuter map". Most notably, the Hutschenreuter map has a large 'blind spot' near the terrestrial southern pole, with the use of free-free emission to constrain the data better [Hutschenreuter and Enßlin, 2020; Hutschenreuter et al., 2022]. This does not disqualify the merits of using the Hutschenreuter map, but should encourage further research into improvements on existing interpolations of the RM sky.

2.2.2 HI and H-alpha Emission Data

Both HI and H-alpha maps of the sky were obtained in the process of data collection. Both maps were used in previous literature to detect HVCs and inform interpolations of the RM sky. In this report specifically, their primary purpose in including them in the collated data is due to display purposes and its potential inclusion in future research.

The HI sky was taken from the HI4PI 21 cm survey, with modifications done by Westmeier [2018] to filter for high-velocity HI sources (above a column density of $2 \times 10^{18} \mathrm{cm}^{-2}$). This modification allows for the better detection and viewing of HVCs in the sky.

The H-alpha sky was taken from Finkbeiner [2003], which was a collage of three smaller H-alpha surveys. Unfortunately, this map is also limited by the same problems as the Hutschenreuter map, with a notable lack of coverage near the terrestrial south pole. It was decided that the H-alpha map would be included in the process of collation for the purposes of future research potential, for example, improving interpolation models like in Hutschenreuter et al. [2022]; Hutschenreuter and Enßlin [2020].

The flux distributions of both HI and H-alpha are shown in figure 2.2. Both distributions appear to follow a poisson distribtion, with the HI data being affected by the central limit theorem.

All data sources collected were first converted to a FITS file under the cartesian projection. The location of individual point-values will not be affected by a cartesian projection, however it can introduce distorions at a high Galactic lattitude. These distortions in data do need to be accounted for.

2.3 Selection of HVCs from the Galactic All Sky Survey (GASS)

HVC-specific data was obtained from Moss et al. [2013] (hereafter referred to as the "Moss catalogue") – a catalogue of all HVCs found using GASS. The Moss catalogue is a primary source of data, for the location and size analysis of HVCs.

The Moss catalogue includes a total of 1693 HVCs, of which most are not viable candidates for analysis. There are several reasons why a particular HVC may introduce significant analysis errors. The first consideration is size. Exceptions to halo HVC sizes cannot be included in HVC analysis as they may not be representative of a typical HVC. For example, the Smith Cloud, due to its size, has an abnormally large corresponding magnetic field. Thus, HVCs that were not in an apparent area range of $(1, \pi)$ degrees squared were masked out. The lower limit exists to guarantee that there are enough RMs covering the cloud itself. This reduces the sample to 151 HVCs.
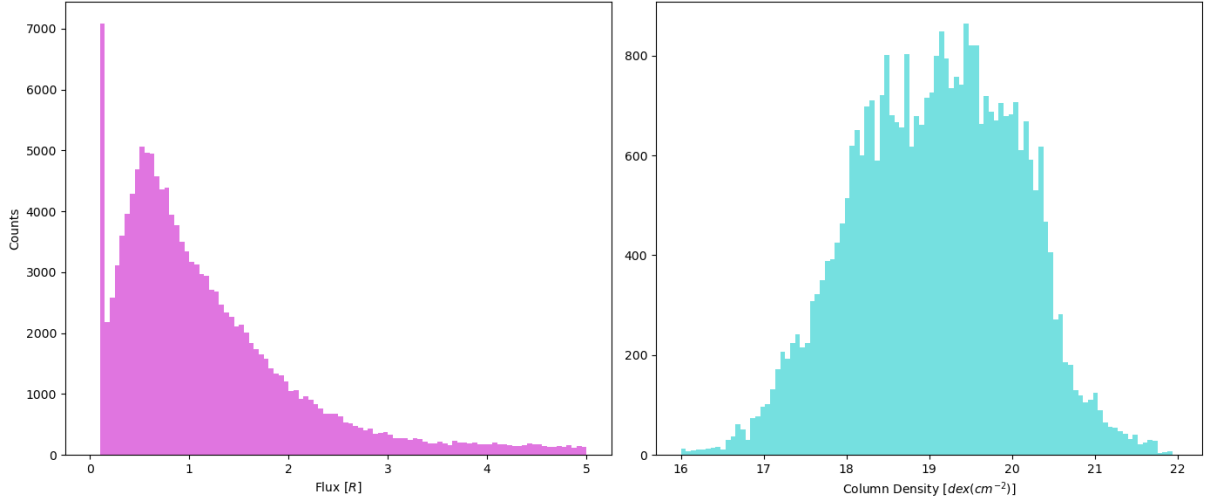
Figure 2.2: Histograms representing the intensity of observed H-alpha (Left) and HI (Right) observations from Beck et al. [2012] and Westmeier [2018] respectively. The HI histogram specifically removes zero-flux observations.

Other considerations made when filtering HVCs were their overlap with the current POSSUM RM grids. Not every HVC is properly covered by the current RM grid. HVCs were filtered out if their centres (obtained from the Moss catalogue) were more than one degree separated from the nearest RM sampling point. This further reduced the sample size to 26 HVCs.

There is a major increase in scatter with POSSUM RMs and interpolated RMs closer to the Galactic midplane [Schnitzeler, 2010]. This is explored in later sections; however, figure 2.3 represents this scatter. Because of this, HVCs close to the Galactic midplane must be eliminated to reduce scatter – specifically HVCs located with Galactic Latitudes $|b| < 20°$ were excluded. This reduced the sample size to 15.

Cartesian projections can distort data at high Galactic latitudes, resulting in bad data. HVCs located at Galactic latitudes $|b| > 80°$ were also eliminated from the sample set. This removed HVC G298.0-81.7+127 and gave a sample size of 14.

Lastly, it was clear that HVC G282.3-38.3+117 had no detectable HI emission according to the provided HI data. It was removed on the basis that it could not be analysed properly. This reduced the final sample to 13 HVCs.

2.4   Data Collation

Once the data was obtained, calculations were done using the `astropy.wcs` pipeline. For every RM point in the sky, the estimated foreground RM from the Hutschenreuter map, the HI column density, and the H-alpha flux, including all associated errors were
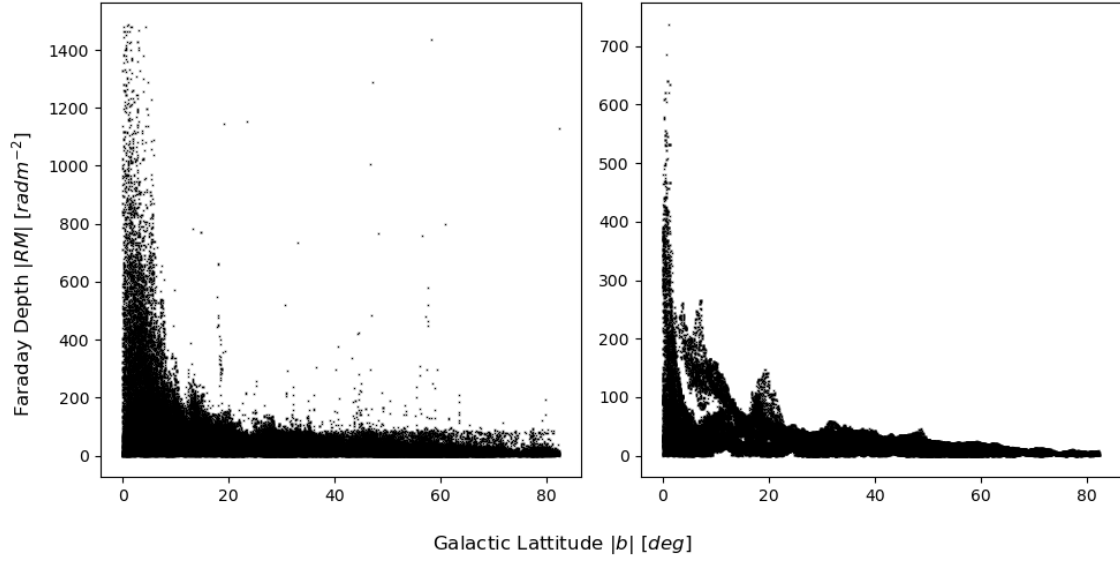
Figure 2.3: (Left) A graph of all ∼180000 RMs plotted against their corresponding Galactic lattitude; (Right) The corresponding graph of all Hutschenreuter map faraday depths matched to the POSSUM RMs. Both graphs represent a significant level of scatter present in RMs collected near the Galactic midplane.

attached to that particular RM sampling point.

2.4.1 HVC Image Overlays

For each HVC, the HI, H-alpha, Hutschenreuter map, and RM grid was 'cropped' to a field twice the size of the maximum HVC source x and y extents. This allows for analysis of both RMs in the HVC and surrounding the HVC.

Foreground Subtraction

Foreground subtraction remains an open question in the field of RM radio astronomy. Due to the inherent magnetisation of the Galactic halo and the ISM, as discussed in sections 1.2.1 and 1.2.2, there are significant contributions to observed RMs from the Galactic foreground across the entire sky. To correctly determine the magnetic field surrounding objects of interest, one must first remove this source of systematic error.

A prime example of the consequences of not correctly accounting for foreground RM contributions is the paper by McClure-Griffiths et al. [2010], which attempted to estimate the magnetic field strength surrounding HVCs in the Leading Arm. However, as from Jung et al. [2021], this result is possibly erroneous due to the obstruction of the nearby Antila supernova remnant region. While the analysis of multiple HVCs is more likely to prevent these errors from compounding to invalidate the conclusions of the report, it is still useful to account for these contributions as much as possible.

3.1 Foreground Reconstruction via Interpolation

All previous work on magnetic field analysis of HVCs, and more broady on radio objects of interest, involve the use of interpolation [Moss et al., 2013; Betti et al., 2019; Westmeier, 2018; Hill et al., 2013; Anderson et al., 2024]. Interpolations are beneficial due to their ability to convert a discrete distribution of RM grid points into a continuous distribution of the RM sky. Interpolations also benefit from a 'smoothing' effect; that interpolated maps can smooth out small-scale imperfections in the RM grid that may not correspond to actual foreground objects [Hutschenreuter and Enßlin, 2020; Hutschenreuter et al., 2022; Khadir et al., 2024]. This smoothing can occur because of the interpolation algorithm itself, or the lack of RM grid density to resolve objects on a particular scale.

The primary issue with interpolation is that they are too effective a technique at reconstructing the RM foreground. Despite the smoothing effects that they can provide, there is no way one can confirm that the RM sky has not included objects of interest as well; an interpolated RM sky could contain the RM profiles of objects of interest. This has the effect of making interpolated maps sourced from high-density RM grids innapropriate for foreground correction, as the original intention of interpolation is to subtract out foreground contributors to RMs – not the objects of interest themselves.

Thus, with the increased RM grid density afforded by the POSSUM survey, and future SKA-era projects, it is of high importance that discussions on how to account for these issues can be solved.

3.2 Annulus Subtraction

The immediate alternative is annulus subtraction. This is a method employed across all fields of astronomy, including radio astronomy, being most applicable to single-object analysis. The method generally involves selecting a series of RM sampling points surrounding any given central RM grid point, averaging the selected RMs, and subtracting the average from the central RM grid point.

There are two sub-methods to consider when performing annulus subtraction: fixed-size annulus subtraction and fixed-sampling annulus subtraction. Fixed-size annulus subtraction involves defining an annulus with a constant inner and outer radius and averaging the RMs exclusively within this radial range. Fixed-sampling annulus subtraction involves defining an inner radius and then selecting a fixed amount of RM grid points that are closest to the central point, but still outside the inner radius. Assuming a constant grid density everywhere in the field, a relationship between the two methods can be quantified, as in equation 3.1.

$$R = \sqrt{r^2 + \frac{N}{\pi n}}$$
$$N = \pi n \left(R^2 - r^2 \right)$$

(3.1)

Where n is the RM grid density in $\deg^{-2}$, r is the inner radius of the annulus in degrees, R is the outer radius of the annulus in degrees (which is directly fixed under the fixed-size regime), and N is the number of RM grid points used (which is directly fixed under the fixed-sampling regime) and is unitless. This means that under a constant RM grid density, these two methods should be approximately equivalent.

There are benefits to both methods. On one hand, fixed-size methods can be described mathematically as convolutions, making them linear. However, they can run into measurement and calculation errors when there is a low amount of RM grid points surrounding the central RM. On the other hand, fixed-sampling methods guarantee a consistent uncertainty and the existence of an average. However, this method is both non-linear and prone to including RM grid points very far away from the central point.

The primary issue with annulus subtraction is determining the size of the annulus, or the amount of RM sampling points to select i.e. what counts as the foreground versus the object, or what is an effective smoothing of the foreground model. This is

Figure 3.1: An Aitoff projection of all portions of the RM sky observed by ASKAP for the POSSUM survey similar to 2.1, filtered through a proprietary fixed-sampling algorithim with inner radius of 0.4" and a samplinig constant of 50.

what leads the above-mentioned errors in both methods. The logical response is either to select a large-area annulus that completely removes the objects' RM contributions (in the case of the sample HVCs this would correspond to an annulus of $1 - \pi$ square degrees in area), or to select a small radius with numerous RM points to capture the foreground contributions both overlapping the object and isolated in the field. Both methods will be analysed in this paper, with the former being discussed in section 3.3.3 and the latter being shown in figure 3.1 [1].

The specific choice of parameters in the fixed-sampling regime being an inner radius of 0.4" and a sample size of 50 grid points – corresponding to an outer radius of approx. $0.728°$. These values were selected to test for small-annulus corrections to RM grid points.

3.3   Fast Fourier Transforms (FFTs)

Many of the methods for foreground subtraction beyond interpolation have a common intersection point in the form of image-based signal processing. Thus, the introduction of Fourier Transforms (FTs) may be a very useful direction for analysis, as they are the foundation for most signal processing methods [Pulfer, 2019]. The benefit of FTs is their linearity, which in several ways can reduce computational expense: the trivialisation uncertainty calculations (quantified in equation 3.3); the linear combination

---

[1]The fixed-sampling annulus subtraction was proprietary data collected from the supervisor. However, the quantitative and qualitative analysis of the viability of this method is my own work.

of several kernel techniques; signal processing in separate orthogonal dimensions; and consistent scaling relationships. FTs also can utilise both convolutional blurring and bandpassing separately, with convolutions already being discussed with annulus subtractions.

FFTs extend the benefits of FTs by providing a FT algorithm of $O(N\log N)$ complexity and allowing FTs to be performed over discrete sets of data. This allows for the analysis of high-definition pixellated images, which is not unlike the standard format and use-case of a FITS file, especially when using a cartesian projection of the sky. Thus, by applying 2-dimensional FFTs to interpolated RM sky images, it is possible to solve the problem introduced by interpolated high-density RM grids.

3.3.1 Non-Uniform Fast Fourier Transforms (NUFFTs)

FFTs can further be extended to the analysis of non-uniform data sets. Standard FFTs rely on the assumption that the grid of sampling points is uniform, and resultantly output uniform-density frequency distributions. NUFFTs do not require the assumption of uniformity, nor do they need to output uniform-density frequency distributions [Bagchi and Mitra, 1996; Greengard and Lee, 2004]. This means that instead of relying on interpolations at all, FTs can be applied directly to the RM grid itself. The primary sources for NUFFTs used in this paper are Bagchi and Mitra [1996]; Greengard and Lee [2004], with heavy reliance on the python module `PyNUFFT` (see appendix D for more).

There are three types of NUFFT: Forward, Adjoint, and "True" [2]. The forward and adjoint types are inverses of each other – forward NUFFTs take a uniform image and a set of sampling points and return a non-uniform frequency distribution. Adjoint NUFFTs reverse that process. True NUFFTs take a non-uniform distribution and output a non-uniform frequency distribution. True NUFFTs are not generally useful for the purposes of this report.

Applying a forward and then an adjoint NUFFT to a set of RM grid sampling points should perform the same task as creating an interpolation. From there, the intermediary step of a bandpass or kernel can be applied to the frequency distribution to produce an interpolation with objects of a particular angular scale removed from the field.

The important first step in determining if this method can create a reliable interpolation on its own. First, an image was selected, specifically a grayscale and cropped image of the Cosmic Microwave Background (CMB) from the Planck mission (see appendix C for more). This was chosen as the test image due to the CMB being able to replicate a noisy and 'blobby' structure, the CMB has also been analysed using FFTs

---

[2]There is no generally accepted nomenclature for type 3 NUFFTs that align with the single-adjective terminology. So "True" is used because it is an accurate descriptor for the type, involving both non-uniform x and k spaces.
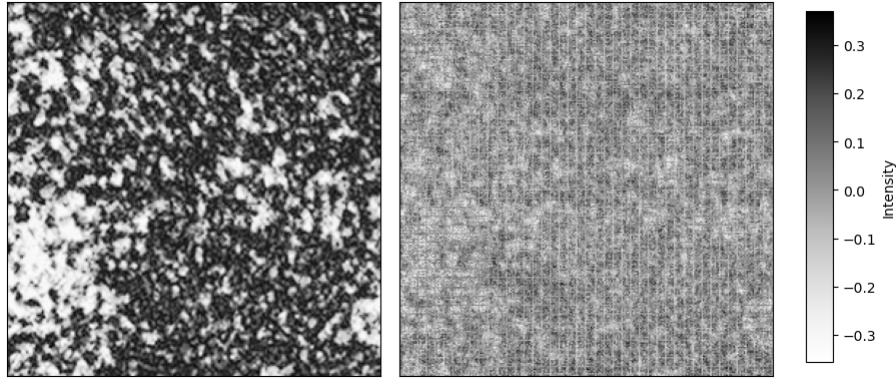
Figure 3.2: (Right) A cropped and grayscale image of the CMB. (Left) The same image after being fed through a forward then adjoint NUFFT. The amount of sample points total to 27000. Both plots share a common intensity colourbar for refrence.

for unrelated cosmological purposes.

Then, a random set of sampling points were selected and treated as the 'mock RMs', with the colour of the background corresponding to the intensity of the RM at that point. The image and the sampling points were then given to the `PyNUFFT` module and transformed in and out of the frequency domain. Figure 3.2 represents the outcomes of this analysis, performed on a sample of simulated RM grids with size $30° \times 30°$. Ignoring the grid-like structure in the recreated image (a consequence of the random point generation algorithm), even with a very high sampling point density or large field, the image is still very low-quality.

This does not disqualify the NUFFT as an analysis technique. Instead, it means that this technique can only work on a very large continuously connected RM set i.e. a complete or partially complete RM grid map of the sky. However, due to the lack of POSSUM data in its early stages, this is a method that must be investigated in the future. Hence its in-depth inclusion in this report despite its apparent shortcomings.

3.3.2   Bandpass Filtering

A simpler method is to directly alter the Hutschenreuter map itself using normal FFTs. First, a 2-D FFT was applied to the Hutschenreuter map. A crosshatch-shaped bandpass was created. This crosshatch imitates a bandpass commonly applied to 1-dimensional signals, where regions of a particular angular area are eliminated by removing all frequencies corresponding to that angular area in the k-space. Equation 3.2 quantifies the relationship between frequency and angular area.

$$k_{\mathrm{HVC}} = \frac{1}{2\theta_{\mathrm{HVC}}R} \tag{3.2}$$

Figure 3.3: Crosshatch-Bandpassed versions of the interpolated RM sky at various opacity gradings - where "original" means 0% opacity. The term "opacity" refers to the effect of the bandpass e.g. 100% opacity means the bandpass completely removes selected frequencies and 50% opacity means that the bandpass halves the presence of selected frequencies.

Where k_{HVC} is the spatial frequency in $\deg^{-1}$, θ_{HVC} is the angular size of the HVC in degrees, and R is the pixel resolution of the axis, in pixels per degree. Assuming all RM sky images exist in a 2:1 cartesian space, due to the range of Galactic latitude and longitude, the value of R is constant across the two axes. The HVC angular size chosen was $1 - \pi$ deg.

The crosshatch is shaped such that, when multiplied by the original k-space, objects of a particular size are either eliminated or reduced in prevalence. This method also guarantees the linearity of the crosshatch 'function'. After this, the inverse FFT is applied to give a resulting foreground map, seen in figure 3.3.

However, bandpassing introduces ripples into the Hutschenreuter map. This effect is expected but undesirable. There are two methods to remove this: either to apply the crosshatch at a certain 'opacity' i.e. the crosshatch is not eliminating all the k-space in its region, but instead is reducing those frequencies by a percentage; or using a more

complex window than a Top Hat, such as a Tukey window or Gaussian window. The effects of the former are seen in figure 3.3. The latter was not investigated due to time constraints.

When applying FTs to any interpolated image, it is important to maintain the corresponding uncertainty map's accuracy. This is where one can take advantage of linearity. Equation 3.3 determines how uncertainties can be calculated.

$$\sigma_{\text{output}} = \mathfrak{F}^{-1}\left[B\big(\mathfrak{F}\left[\sigma_{\text{original}}\right]\big)\right] \tag{3.3}$$

Where $B: \sigma \to \sigma$ is the bandpass function, σ_{output} and σ_{original} is the uncertainty images for the output and input respectively in radm^{-2}, and $\mathfrak{F}$ is the FT.

3.3.3   Kernel Filtering

The same techniques from above can be applied via convolutions, where the aim is to convolve the Hutschenreuter map with a defined kernel. Two-dimensional convolutions have a time complexity of $O(n^4)$, depending on the kernel size, whereas the FFT has a complexity $O(n^2\log^2 n)$. By performing a FFT on both the kernel and the Hutschenreuter map separately, then multiplying the two k-spaces together, and applying an inverse FFT, the result is a faster application of a convolution with a kernel. This was the chosen method to demonstrate the large fixed-size annulus subtraction method, with an inner radius of 1 degree and an outer radius of π degrees Figure 3.4 displays the results of this method.

The main problem is that the annulus kernel appears to blur out smaller-scale structures. This can lead to more minute RM changes smaller than the angular size of the HVC to be removed out when it may be neccesary to keep them.

3.4   Characterising Methods to Improve Interpolations

As seen from figures 1.3 and 2.3, there are several ways in which the RM grid can have 'bad data' – most notably in a lack of signal-to-noise and the inherent scatter when observing near the Galactic midplane. Thus, the final step of this chapter is to both characterise the RM sample set and to compare the subtraction methods against each other.

Figure 3.5 represents a simple residual histogram comparison between all the methods discussed in this chapter. The desired result is seen in the residuals between the interpolated or crosshatch-bandpassed RMs and the actual RMs - appearing as a distribution centred at zero (which does not look gaussian). This is the same for the annulus-bandpassed RMs, and is opposed to the annulus-convolved method, which does not appear to interact with the RM grid in a desirable manner.
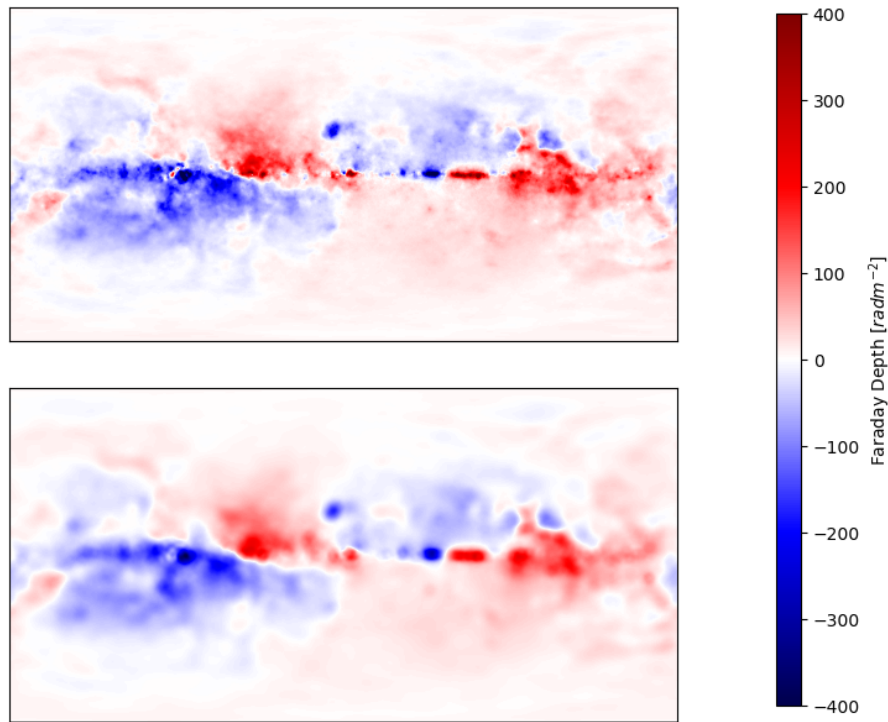
Figure 3.4: Cartesian plots of the interpolated RM sky (Top) compared against the Annulus-Bandpassed version of the interpolated RM sky (Bottom). The annulus kernel used sums to unity, making it act like a unitary operator, standard for blurring techniques [Pulfer, 2019]. The annulus size ranged from 1-π degrees.
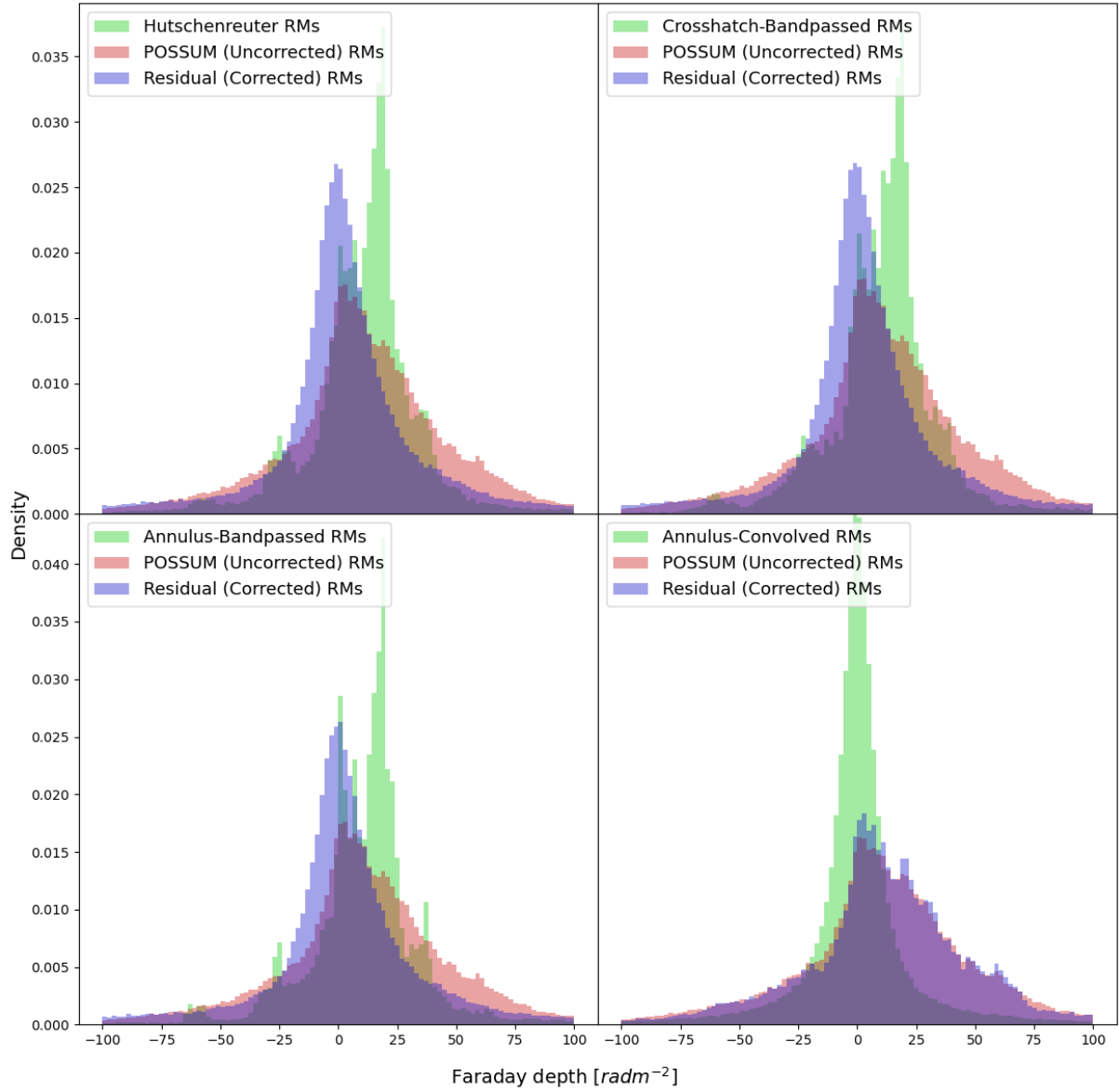
Figure 3.5: Residual histogram plots of the actual POSSUM RMs compared to the corresponding various foreground removal methods: unaltered interpolation (Top left); crosshatch-bandpassed (Top right); annulus-bandpassed (Bottom left); and annulus-convolved (Bottom right).
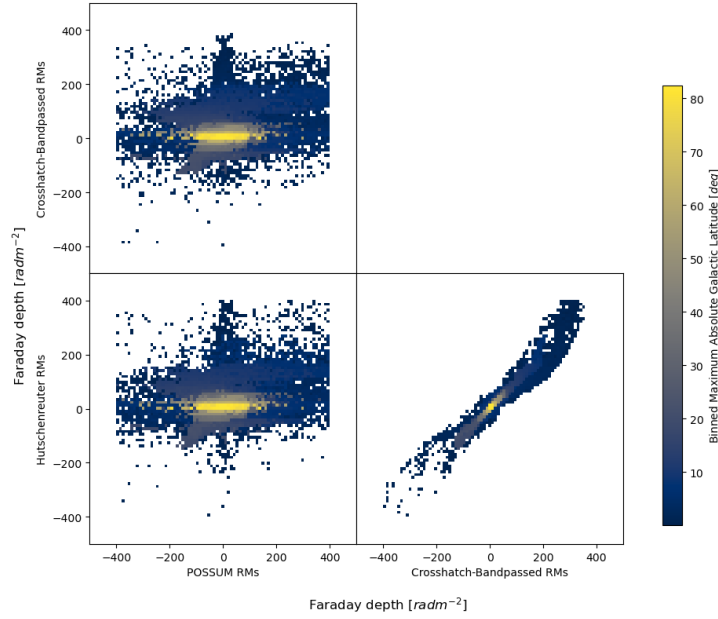
Figure 3.6: Three corner plots of all RM sampling points, describing the relationship between the several associated RM values and the Binned Maximum Absolute Galactic lattitude indicated by colour. Here, a comparison between POSSUM RMs, Hutschenreuter RMs, and Crosshatch-Bandpassed RMs is displayed.

Figure 3.6 demonstrates the similarities between the crosshatch-bandpass and unaltered Hutschenreuter map, with them being related to each other in a linear manner, specifically with a gradient of approximately unity. This is ideal, as it means that the crosshatch-bandpass method is not deviating significantly from the Hutschenreuter map, only altering it subtly. The figure also demonstrates how scattered the RMs become near the Galactic midplane, hence it being plotted for colour to delineate between RMs near and far away from the midplane.

Figure 3.7 compares the unaltered Hutschenreuter map with the annulus-convolved method (a.k.a. the fixed-size annulus method). From the bottom two graphs, the annulus-bandpass is similar to the crosshatch-bandpass, leaving most RMs as correlated.

Figure 3.8 compares the unaltered Hutschenreuter map with the annulus-convolved method (a.k.a. the fixed-sampling annulus method). There is a somewhat linear relationship between the actual RMs and the annulus-convolved RMs, ignoring the heavy scatter closer to the midplane. From all three maps, it appears that there is not much of a correlation between the Hutschenreuter and POSSUM RMs. This implies a lot of smoothing is already performed by the Hutschenreuter map, as anticipated in section 3.1.
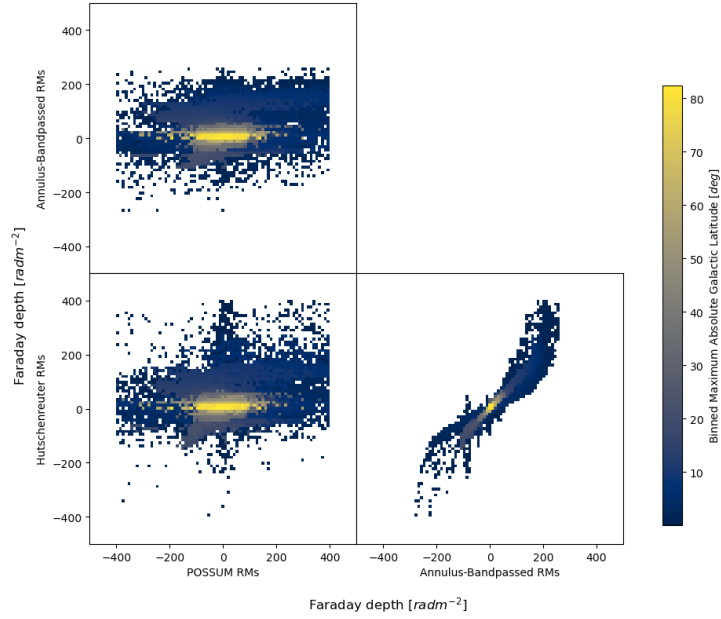
Figure 3.7: Three corner plots of all RM sampling points, describing the relationship between the several associated RM values and the Binned Maximum Absolute Galactic lattitude indicated by colour. Here, a comparison between POSSUM RMs, Hutschenreuter RMs, and Annulus-Bandpassed RMs is displayed.
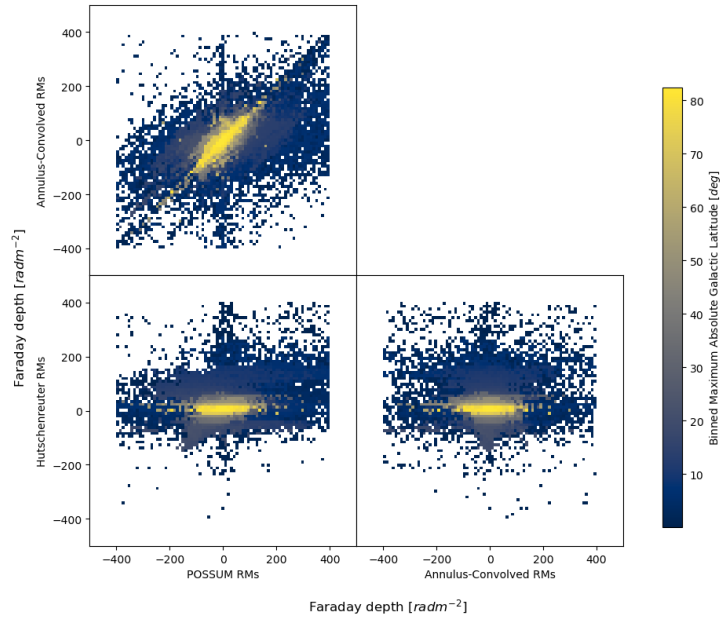
Figure 3.8: Three corner plots of all RM sampling points, describing the relationship between the several associated RM values and the Binned Maximum Absolute Galactic lattitude indicated by colour. Here, a comparison between POSSUM RMs, Hutschenreuter RMs, and Annulus-Convolved RMs is displayed.
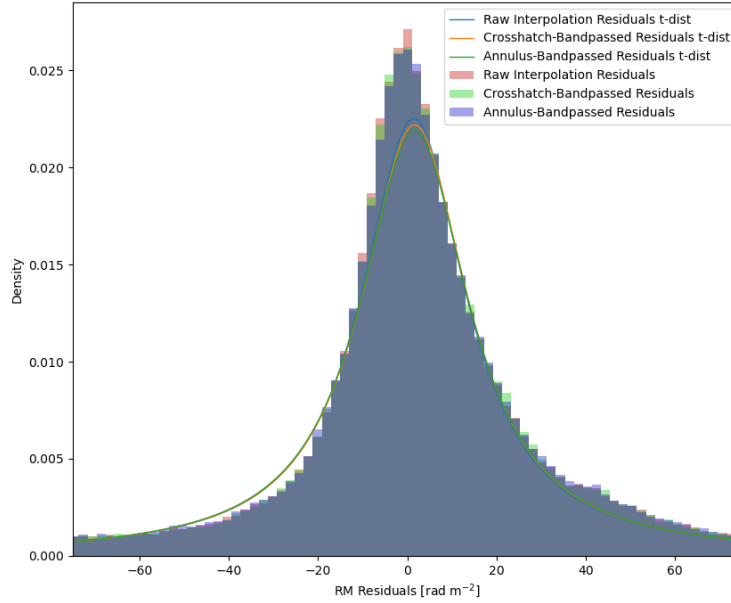
Figure 3.9: The sample of all RMs corrected with the Hutschenreuter Interpolation (Blue) and Crosshatch-Bandpassed Interpolation (Red). A bootstrap fitted t-distribution is drawn on the graph for each respective residual RM set.

3.5 Statistical Comparison of Foreground Removal Methods

The corrected RM histograms for both bandpass methods displayed in figure 3.5 do not follow a Gaussian distribution or a Cauchy distribution, but do follow a Student's t-distribution. This has been seen before in past analysis of residual RMs [Anderson et al., 2024]. By eye, it is quite clear that this is not the case for the annulus-convolved method, hence why no statistical analysis was conducted on it beyond an R^2 calculation. A chi-squared test can be used to compare the residual RM distributions with the t-distribution, with the t-distribution being fitted via a bootstrapping method. 1000 resamplings with replacement were used. Table 3.1 displayed the resulting t-distribution fit and Pearson's chi-squared statistic, which tests for similarity instead of difference. The p-values for both were extremely small, despite the clear visual incongruency in the model and data set in figure 3.9. This is most likely caused by the t-distribution fitting very well with the tails and mid-section of the histogram.

The Pearson R^2 test can be performed in comparing the Hutschenreuter map with its corrected versions. This includes the annulus-convolved method despite a greater visual correlation with POSSUM RMs from figure 3.8. Ideally, the R^2 statistic should be somewhat close to 1, as not a lot of sub-degree variations are expected (due to the single-degree scales of the Hutschenreuter map's sources). Table 3.1 presents the R^2

Residual Set	t-Distribution Fit		
	Centre	d.o.f.	Scale
Straight Interpolation	1.461 ± 0.190	1.040 ± 0.0039	14.24 ± 0.0606
Crosshatch-Bandpassed	1.648 ± 0.047	1.046 ± 0.0039	14.47 ± 0.0608
Annulus-Bandpassed	1.617 ± 0.195	1.054 ± 0.0040	14.67 ± 0.0630

Residual Set	χ^2 **Results**	
	Statistic	p-value
Straight Interpolation	0.01432	1.0442E-166
Crosshatch-Bandpassed	0.01460	2.671E-166
Annulus-Bandpassed	0.01385	2.105E-167

Methods	R^2 **Statistic**
Interpolation vs. Crosshatch-Bandpassed	0.9279
Interpolation vs. Annulus-Bandpassed	0.8701
Interpolation vs. Annulus-Convolved	0.003866

Table 3.1: (Top) Student's t-distribution fit parameters for the residual histograms as displayed in figure 3.9. (Middle) Results of the χ^2 test comparing residual histograms with the t-distrubution. (Bottom) R^2 statistics comparing the Hutschenreuter map with the other methods detailed in this section.

statistics for a series of compared cases.

3.6 Other Methods

There are other methods for foreground removal were not considered viable options or of enough importance to numeerically analyse in this report. However, they may still offer useful methods for future researchers. The first is median filtering, which is like previously discussed convolutional blurring methods. Huang et al. [1979] provides a description of a fast median filtering algorithm for two-dimensional images. Arias-Castro and Donoho [2009] is also a reference describing the potential benefits of median filtering, including a more robust removal of noise due to the robust statistical properties of the median. It was disregarded in this report due to its inherent non-linearity, leading to more computational complexity, and the debatable nature of whether this disadvantage is worth the advantages it can bring. Linear decomposition of line-of-sight RMs are also possible, attempted in Schnitzeler [2010]. However, it is also quite mathematically complex and may not be conducive to a generalised algorithm, hence the lack of focus on this technique in this report. Despite the methods presented in the report, in section 4, a non-altered Hutschenreuter map will be used with the justification found in section 4.3.

Analysis and Results

In constructing an algorithm to detect the signature of, and to further estimate the strength of magnetic draping in HVCs, as in section 1.5, it is important to pay attention to the validity of the methods being employed, as there has been no well-established precedent for doing so on large samples of HVCs.

4.1   Kolmogorov–Smirnov (KS) Testing

Before estimating the strength of the magnetic draping signature on HVCs, it is important to first confirm that there is a detectable magnetic field to analyse. To do this, the KS test was employed. The set of RM grid points for each HVC collated in section 2.4.1 include any grid point within $2\delta x$ degrees of the HVC centre, where δx is the HVC angular diameter, the average value between the Moss catalogue's 'dx' and 'dy' values (i.e. its cartesian dimensions), shown in appendix table A and in figure 4.1. Two separate populations can be formed by delineating RMs inside and outside a distance δx from the HVC centre. All sampling points within the defined circle makes the "HVC RMs" population, and the ones outside the circle makes the "Background RMs" population.

An assumption is made here that HVCs can be represented by a circular region in the sky. Allowing for methods to distinguish between the surrounding backgrounds and HVC RM grids. As seen from the HI plots in figure 4.1, this assumption appears to only be correct in particular cases. But do note that the HI background discriminates for high-VLSR HI emission. The HI background is a visual tool, and it cannot be used as a one-to-one tracer of ionised gas.

A two-sample, two-tailed, KS test was performed comparing both the background and HVC RM distributions. A critical p-value of 0.001 was assumed to determine if a significant magnetic field was detected. This would correspond to 99.9% significance of difference. Table 4.1 shows the KS test results applied to each HVC. Out of the 13 HVCs tested, 10 HVCs (77%) had a significant difference between both populations in the corrected RM case.

For uncorrected RMs, the KS test determined that 12 HVCs had a significant difference between both populations. No HVC had both a significant detection for the uncorrected case and a non-significant detection for the corrected case. This implies that
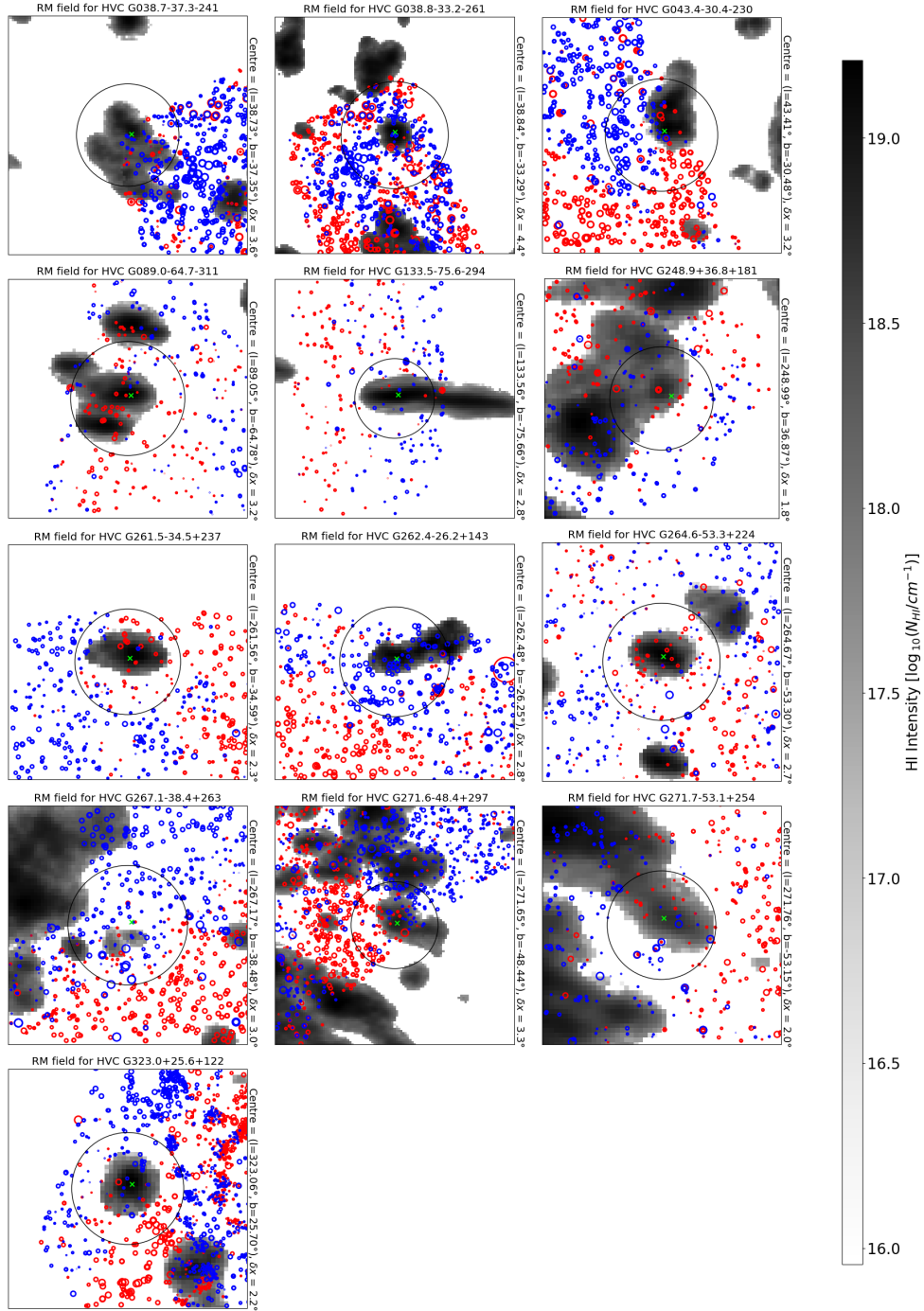
Figure 4.1: All 13 HVCs used in analysis. The HI column density is represented using a greyscale image background. The RMs are represented by circular markers, their size equal to the magnitude and the colour representative of their sign with red being positive, and blue being negative. The black circle is the deliniation between in-HVC and out-HVC populations, and the green 'x' indicates the centre of the HVC. Each HVC image includes the centre and the chosen δx value as discussed in section 4.1.
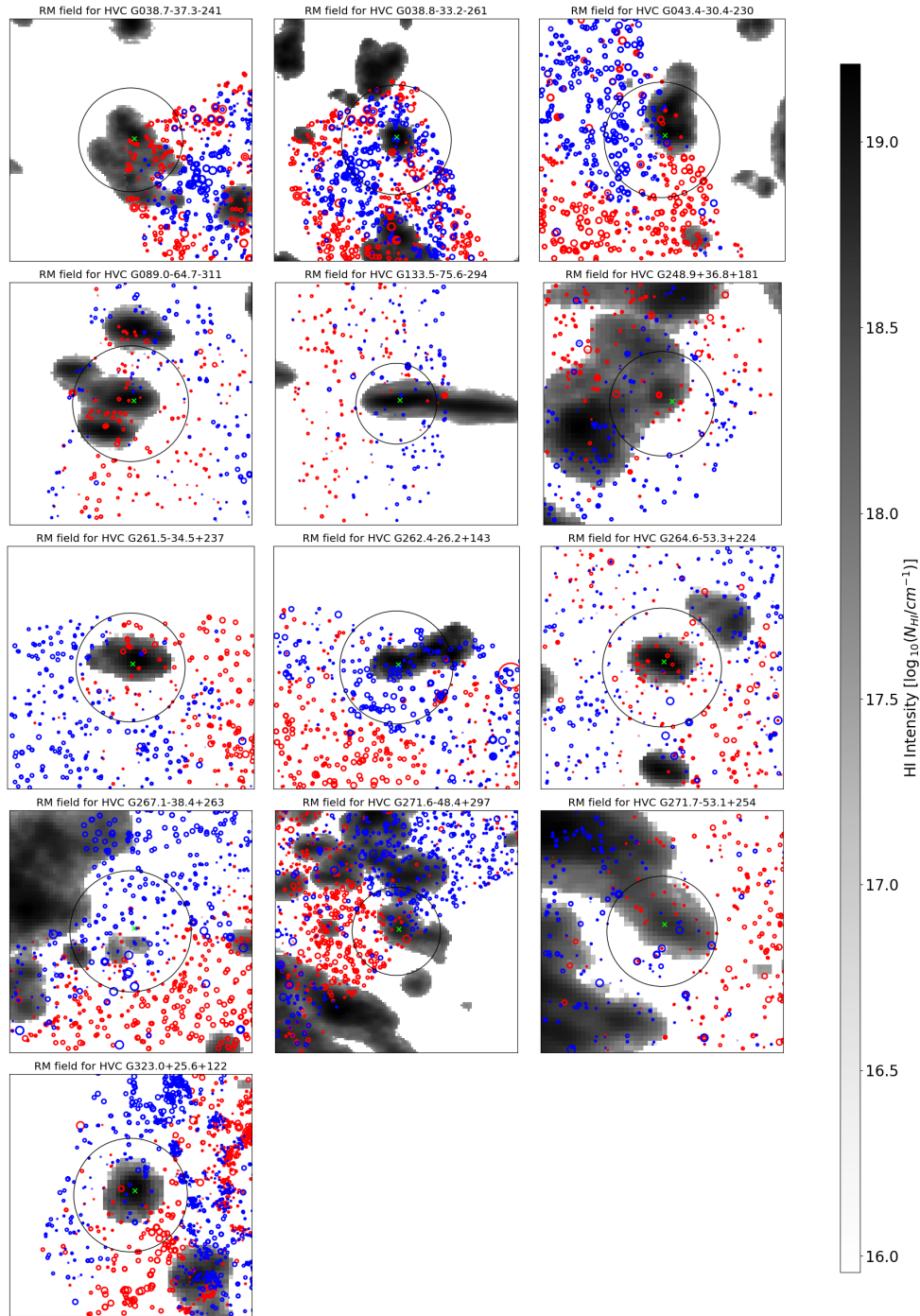
Figure 4.2: The same set of HVCs in HI with RM overlays, displayed the same as in 4.1. However, instead of using the Hutschenreuter map as a method of correction, the mean of the uncorrected RM values in the frame is subtracted out from each RM point.

Name	Corrected RMs		Raw RMs	
	Statistic	p-value	Statistic	p-value
G038.7-37.3-241	0.207	3.52E-09	0.198	1.98E-08
G038.8-33.2-261	0.311	1.39E-08	0.516	8.69E-24
G043.4-30.4-230	0.241	3.61E-11	0.174	5.20E-06
G089.0-64.7-311	0.374	1.51E-02	0.499	2.96E-04
G133.5-75.6-294	0.461	4.57E-08	0.485	6.34E-09
G248.9+36.8+181	0.081	4.53E-01	0.110	1.32E-01
G261.5-34.5+237	0.289	5.96E-08	0.324	6.28E-10
G262.4-26.2+143	0.213	1.22E-06	0.221	4.48E-07
G264.6-53.3+224	0.320	4.07E-05	0.346	6.04E-06
G267.1-38.4+263	0.343	2.32E-11	0.348	1.14E-11
G271.6-48.4+297	0.125	5.09E-05	0.155	1.69E-07
G271.7-53.1+254	0.227	3.40E-04	0.246	7.62E-05
G323.0+25.6+122	0.099	1.51E-02	0.187	4.79E-08

Table 4.1: A table describing the KS test results for each HVC.

using the corrected RMs makes the KS test more selective. The use of the Hutschenreuter map is justified as it means false positives are less likely to appear.

There appears to be a moderate correlation between the KS statistic and the absolute Galactic lattitude for each HVC, with a calculated R^2 statistic of 0.6039. When determening correlation with respect to p-value instead of KS statistic, the R^2 statistic drops to 0.4489. The KS test does not appear to be correlated with VLSR or VGSR, having an R^2 statistic of 0.03023 and 0.008367 respectively.

4.2 Assumptions

Due to the significant limitations in available data, the use of assumptions is necessary to lay the groundwork for increasingly robust analysis. Without assumptions, it becomes difficult to construct methods for the estimation of magnetic fields. Hence, the four primary assumptions below allow for the formation of a working method, with the explicit description meant to point to how the method can be improved.

The first major assumption is that the ionisation fraction of the Galactic halo is approximately constant, i.e. gas in the halo is well-mixed. This does not account for major sources of heterogeneity caused by HVCs (a desired outcome) or other ionised regions such as the Magellanic Clouds (an undesired outcome).

Simulation data can be used to analyse the problematic nature of assuming a constant ionisation fraction [Grønnow et al., 2017]. However, it is difficult to apply simulation data to observational data due to the amount of variables that need to be

controlled for. Similar to the method employed in Grønnow et al. [2017], it will be assumed that the ionisation fraction is high and constant.

The second major assumption is that the weighted average of the HI column density on a HVC is linearly proportional to, and biased towards the peak column density in the centre of the HVC. This is an approximation that aims to simplify calculations to the analysis of a single data point provided in the Moss catalogue. A more complex estimation of average HI column density requires a significantly more in-depth analysis. HI column density is certainly not uniform within clouds, as mentioned in Heitsch et al. [2021]. It also neccessitates some level of correlation between line-of-sight magnetic fields and their uncertainties (a consequence of Poisson noise).

Both above assumptions sacrifice accuracy for simplicity, and is allowable primarily due to the method of calculation explained by Kaczmarek et al. [2017] and in section 4.3. In this report, the simplicity does not disqualify the results of the investigation, but it does remove its ability to be definitive. The result of applying both assumptions is that the line-of-sight magnetic field strength is linearly proportional to the faraday depth with a scaling constant unique to each HVC – as demonstrated in section 4.3.

The third assumption was the same one employed in section 4.1 - that HVCs appear as approximately circular in the field of view. All three additionally meet the desired goal of creating method that can adapted and refined for future use. As discussed in sections 5.2.2 and 6, all three assumptions can be dropped in the presence of more detailed data or more rigorous methodologies manipulated from the one described in this paper. Lastly, a very typical assumption made is that the RM contribution along a line of sight is added along said line of sight. This is not necessarily correct; however, it is a fair assumption that most past literature has made to deconstruct equation 1.2 [Kaczmarek et al., 2017; Moss et al., 2013; Hill et al., 2013]. This makes the fourth assumption.

4.3 Derivation of Line-of-Sight Magnetic Fields

As from equation 1.2, there is a relationship between the line-of-sight magnetic field and the faraday depth. By removing foreground contributions to the faraday depth, one can isolate the specific contribution of the line-of-sight magnetic field made by the HVC. At the same time, the fourth assumption can be used to solve the integral in equation 1.2, resulting in equation 4.1 [Hill et al., 2013].

$$\frac{\left\langle B_{\parallel} \right\rangle}{\mu \mathrm{G}} = \frac{\left\langle RM_{\mathrm{cor}} \right\rangle}{0.81 \left\langle n_e \right\rangle L_{H^+}} \tag{4.1}$$

Where $\left\langle B_{\parallel} \right\rangle$ is the average line-of-sight magnetic field in μG, RM_{cor} is the cor-

rected RM in radm^{-2}, n_e is the electron density in cm^{-3}, and L_{H^+} is the HVC ionised path length in pc. From this equation, Kaczmarek et al. [2017] derives a simplified equation that eliminates the need to calculate the electron density and ionised path length, as seen in equation 4.2.

$$\frac{B_{\parallel}}{\mu\mathrm{G}} = 3.80 \times 10^{18} \frac{RM_{\mathrm{cor}}}{X \langle N_{HI} \rangle} \tag{4.2}$$

Where X is the unitless ionisation fraction, and $\langle N_{HI} \rangle$ is the weighted average HI column density over the region being analysed, measured in cm^{-2}. This equation can only be derived under the first assumption. Additionally, the use of the average HI column density is intrinsically tied to the second assumption.

Applying both assumptions one and two and utilizing equation 4.2 demonstrates that the line-of-sight magnetic field is linearly proportional to the faraday depth. Thus, an RM denoting the singular faraday depth associated with any given HVC, and any given background surrounding the HVC. These two RM values can be subtracted from each other and converted into a magnetic field via multiplication of a constant factor to create what is refered to as the 'master RM'.

Despite the detailed analysis conducted in section 3, it was decided that the non-altered Hutschenreuter map be used to correct RM contributions. This is due to most already-existing literature relying on interpolations. From figure 4.3, which displays histograms of the corrected and uncorrected line-of-sight magnetic field points surrounding HVCs, it is demonstrated that the Hutschenreuter map can remove the anisotropy of the ISM by turning an uncorrected bimodal symmetric distribution into a t-distribution centred at zero.

Figure 4.1, presents HI images of all 13 HVCs and the overlapping RM grids. The filtered Moss catalogue, including all 13 HVCs is displayed in appendix B. It is apparent that once the foreground is removed, ridge-like structures appear in the data which may correspond to the turbulent mixing of gas in the halo [Heitsch et al., 2021; Mao et al., 2010].

4.4 Mathematical Methods to Evaluate HVC Magnetic Fields

It is highly important to seperate the techniques performed in this section, as opposed, to the detection method outlined in section 4.1. A faliure of the methods described here to significantly determine the strength of the magnetic fields do not imply a faliure in detection of a magnetic draping signature. This is further elaborated in the discussion section 5.2.4. This is important to point out given the size of the uncertainties in table 4.2 being large enough to reasonably have a magnetic field value of zero.
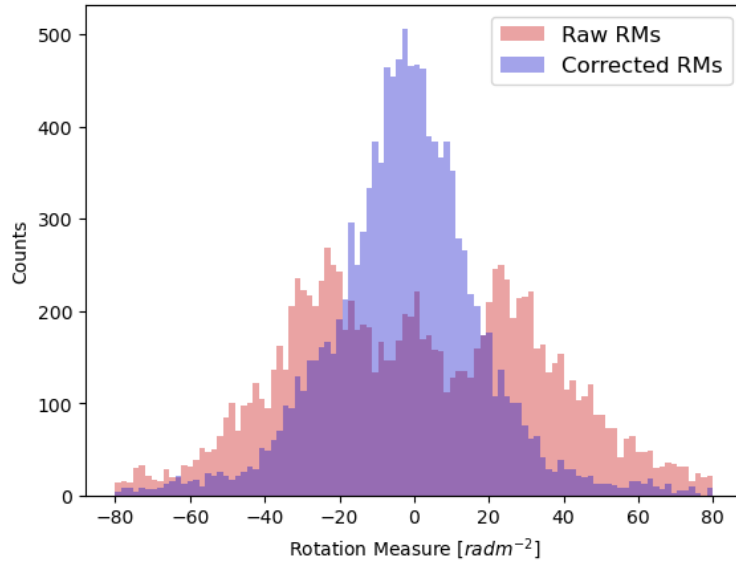
Figure 4.3: Two histograms describing the RM sample within a certain distance to the 13 sample HVCs. The red histogram uses uncorrected RMs. The blue histogram uses corrected RMs.

For the HVCs which did have detectable magnetic fields, the next step is to estimate the strength of the magnetic field draping over each HVC. Previous analyses of the Smith Cloud, such as in Betti et al. [2019]; Hill et al. [2013], utilises a weighted average of RMs to obtain the 'Master RM'. This may not be transferable to a generalised algorithm. While the background RM population will generally follow the expected normal distribution, the in-HVC population distributions can vary depending on the orientation of the HVC with respect to the observer. For more face-on HVCs, RMs may form a ring of RM values ranging from positive to negative around the ring, resulting in a zero weighted average. These can also be refered to as 'coffee stain' RM fields.

In Betti et al. [2019]; Hill et al. [2013], due to analysing one single and large object, it is possible to divide the object into several smaller sections for analysis. It is not possible to do this especially given the limitations created by assumption three.

The more complex HVC RM distribution combined with the oversimplified spherical morphological model means that using a weighted average may underestimate strengths - the same applies to most forms of modal analysis including gaussian fitting i.e. any method that can not account for antimodal or multimodal analysis. This report proposes two new methods to determine the magnetic field strength surrounding HVCs under the simplified spherical morphological model, which can overcome the potential issues with the weighted average. Sections 4.4.1 and 4.4.2 attempts to justify the mathematical validity of these two methods, and section 4.5 shows both the results of using these methods, with some further post-hoc justifications demon-

Figure 4.4: A diagram representing the physical intuition of the KS-EDF method. The graph shows the EDFs of inside and outside populations for an example HVC. The lines drawn on the diagram represent the statistic value and the KS-EDF 'master RM' value.

strated via statistical analysis in 4.5.2.

Despite the potential shortfalls of the weighted average, it is a method that is sanctioned by literature and is still a valid method to use and compare other methods to. It is only an important limitation to pay attention to in the analysis of HVCs.

4.4.1 KS-EDF Method

The first proposed method relies on both the results of the KS test and the Empirical Distribution Functions (EDFs) of the in-HVC and out-HVC populations required to evaluate the KS statistic. The x-axis location of the KS statistic is where the distribution of the two populations differ the greatest. And thus, it is not unreasonable to state that the magnetic field strength corresponds to this location in some manner. This is shown in figure 4.4, where the red line denotes the KS statistic's length and x-axis position.

The second step in this method is to further remove background interference as explained in section 4.3. This can be done by finding the x-axis location at which the density in the background population EDF equals that of the density of the HVC population EDF at the KS-derived x-axis location. This step has the effect of removing any potential deviation from zero that the magnetic field in the background has due the ridge-like structures, which will appear in the EDF as either (i) any deviation from a standard normal distribution, or (ii) a deviation from the centre of the normal

distribution as a function of its uncertainty.

This is shown in figure 4.4 with the black line – the length of the black line representing the final assessed magnetic field value. In this case, the background population in orange is approximately normal. So, case (ii) from the paragraph above is demonstrated.

The second step is not always valid, as RM values can vary due to turbulence, creating an inherent variability in the EDFs. Hence the necessity of further statistical analysis.

4.4.2   Variance Subtraction

Another method involves the reverse-propagation of uncertainties. An assumption can be made that for some HVCs, there is an inherent variation in the magnetic field as one looks at different locations in the defined morphological circle, appearing as the afformentioned 'coffee stain' shape. This inherent variance is denoted as σ_{true}^2.

Additionally, each RM measurement comes with a measurement uncertainty, denoted as $\sigma_{\text{meas.}}$. Propagating these two uncertainties would give what should be the observed variance, σ_{obs}^2, as shown in equation 4.3.

$$\sigma_{\text{obs}}^2 = \sigma_{\text{true}}^2 + \sigma_{\text{meas.}}^2 \tag{4.3}$$

The observed uncertainty can be calculated by taking the statistical standard deviation of the population. The measurement uncertainty can be averaged to give a whole-population measurement uncertainty approximation. This allows for equation 4.3 to be reversed to derive the 'true' variance in the RM population - see equation 4.4.

$$\sigma_{\text{true}} = \sqrt{\text{Var}\left(\text{RM}\right) - \langle\sigma_{\text{RM}}\rangle^2} \tag{4.4}$$

By definition of standard deviation, the corresponding true variance can be approximated as the average separation between RMs in the population, thus quantifying the inherent variation in the HVC magnetic field, i.e. the magnetic field strength.

The same can be done to the background population, instead to detect the potential interferences of the ridge-like structures of the halo magnetic field. This can be used to subtract out the background interferences that were included in the derivation of the true in-HVC variance.

A clear potential source of error in this method comes in the fact that the standard deviation is positive, affecting the validity in two separate ways: (i) cases where the average measurement uncertainty is larger than the statistical standard deviation, resulting in a non-real uncertainty; (ii) cases where the line-of-sight magnetic field strength *should* be negative but is calculated as positive (before the true background variance is subtracted) i.e. the field vectors point away from the telescope. Case (i)

Name	Abs. Magnetic Field $|B_\parallel|$ (µG)		
	Wgt. Avg.	KS-EDF	σ-Sub.
G038.7-37.3-241	2.56± 1.88	1.15± 1.12	1.17± 1.07
G038.8-33.2-261	1.25± 1.26	0.36± 0.75	1.13± 0.70
G043.4-30.4-230	2.30± 1.75	0.31± 0.93	1.61± 0.93
G133.5-75.6-294	1.79± 1.54	1.24± 1.29	0.76± 1.27
G261.5-34.5+237	7.08± 8.70	3.88± 4.55	3.39± 4.39
G262.4-26.2+143	5.01± 6.13	10.93± 8.64	3.94± 2.77
G264.6-53.3+224	2.12± 3.44	0.11± 2.58	2.18± 2.26
G267.1-38.4+263	9.41± 6.69	3.84± 3.73	3.48± 3.29
G271.6-48.4+297	0.59± 1.98	0.13± 1.24	0.08± 1.21
G271.7-53.1+254	2.40± 3.60	0.57± 2.43	0.02± 2.22

Table 4.2: A table describing the magnetic field derivations for each HVC. HVCs from the sample of 13 that had no significant KS test detection, or an invalid variance subtraction result are removed.

does not invalidate the method outright but does mean that 'bad data' had to be thrown out. This happened in only one case as seen in section 4.5. Case (ii) is irrelevant in the conclusion, as the parity of the magnetic field is not a factor being analysed. However, if the main concern is if the background and HVC true variances differ in sign. This is not of concern because if there is a sign difference, the background ridge-like structures would cancel-out the presence of HVC magnetic fields, resulting in every invalidating occurrence of case (ii) necessarily leading to case (i).

To reiterate, the caveats and assumptions described in this derivation may appear as mathematically or intuitively valid, however it is worthwhile to test things via statistical analysis and modelling (see section 5.2.4).

4.5 Magnetic Field Results

The results of each method are compiled in table 4.2.

The distributions of the results are displayed in the boxplots of figure 4.5. The Smith Cloud magnetic field as discussed in section 1.4 is marked with a red line, and the upper bound as discussed by the Grønnow et al. simulations in section 1.2.1 is marked in blue. Both values at 8 and 3 µG respectively act as suggested upper bounds for the strength of these HVCs.

From figure 4.5, the magnetic field strengths are overall higher compared to the hypothesised estimate of being on the order of magnitude of 0.1 µG from the Grønnow et al. simulations. The three methods appear to visually agree with each other approximately, with the KS-EDF having a generally higher estimate for the magnetic
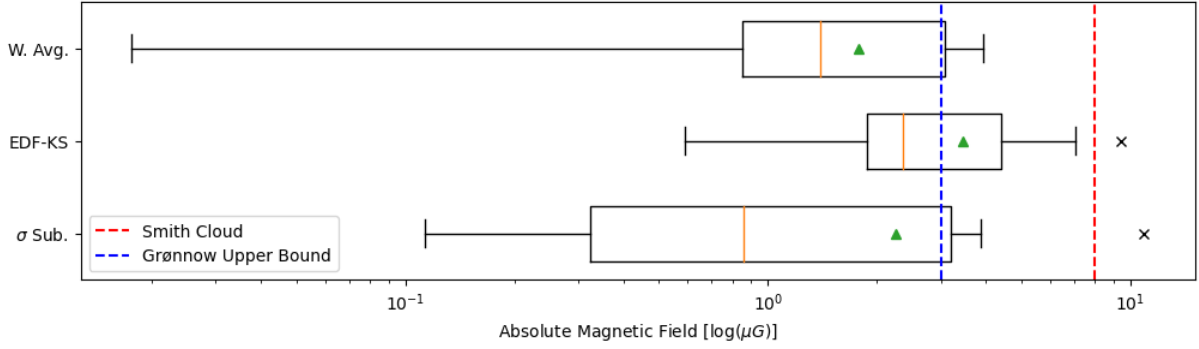
Figure 4.5: A boxplot representing the absolute-value magnetic field of each HVC for both derivational methods. The red and blue dotted lines indicate two predicted upper bounds, one set by the Grønnow et al. simulations, and the other by the Smith Cloud respectively. Displayed is the mean (green triangle) and median (orange line) for each method of evaluation.

field value, the Variance Subtraction having the greatest spread, and the Weighted Average having the largest tail. It is important to note that due to the logarithmic scale used, the mean is inherently biased to visually appear at higher values. However, the use of a logarithmic scale is still justified due to the order-of-magnitude levels of error.

4.5.1 Uncertainties

With each method comes a unique derivation of uncertainties. The uncertainty in the weighted mean is given as trivial – calculated separately for the HVC and background populations, and then propagated. When calculating RM uncertainties, an intrinsic uncertainty of 7 radm^{-2} must be added. This value comes from Schnitzeler [2010], being the extragalactic radio source scatter, post-correction.

The uncertainty in the KS-EDF statistic reflects the inherent variability in the method and is calculated by the Euclidean addition of the average measurement uncertainty of both the HVC and background populations. This corresponds to the propagation of RM uncertainties shown in figure 4.4, where the black line considered to vary as the EDF varies in shape from resampling. The uncertainty in the variance subtraction method was estimated via bootstrap resampling with replacement. The number of samples generated per population is equal to the size of the population being analysed. Once the HVC and background population uncertainties were evaluated, the two uncertainties were propagated to produce the listed result.

Note that when uncertainties are greater than the magnetic field values, as seen in table 4.2, it does not mean the detection is invalid, but that the stated method cannot confidently estimate the field strength. This comes back to the understanding that the assumptions greatly decrease precision, but that these values can be improved.

Methods		Difference (µG)			p-value
		Mean	Upper Bd.	Lower Bd.	
Var. Sub.	KS-EDF	-1.199	-2.783	0.3853	0.8259
Wgt. Mean	KS-EDF	-1.675	-3.259	-0.09067	0.9643
Wgt. Mean	Var. Sub.	-0.476	-2.06	1.108	0.2455

Table 4.3: A table describing the Tukey Multiple Comparison of Means test results for the HVCs with magnetic field detection.

4.5.2   Statistical Comparison of Methods

Two statistical tests were used to compare the three methods' derived magnetic field values (instead of master RM values, which is linearly proportional to the magnetic field value due to assumption 2). A weighted ANOVA test was employed as it can compare multiple methods against each other, with the weights allowing for the accounting of uncertainties. The F-Statistic calculated from the weighted ANOVA test was 3.375, with a corresponding p-value of 0.0388, meaning there is only a 95% confidence interval of similarity, but is still fairly weak. See appendix E for further detail.

The weighted ANOVA test results were also fed into a Tukey multiple comparisons of means test. The results of this test are shown in table 4.3. Note that here, the p-value is a measure of the likelihood that the two data sets are different. It is clear that an alternative hypothesis, that two given distributions are different, is not met to 95% confidence in all cases except when comparing the weighted mean and KS-EDF method. However it is clear that the KS-EDF method does not match well with the other two cases in-general. To better quantify the agreement between the weighted mean and variance subtraction methods, a reduced chi-squared statistic was calculated using the independent propagation of uncertainties. The resulting reduced chi-squared statistic was 1.088 - which is very close to an ideal value of unity.

The reason for the weighted ANOVA test as a whole giving a weak significance of similarity compared to only one of three values in the Tukey test giving strong evidence of similarity, is due to the ability of the weighted ANOVA test to 'bridge the gaps' created by two data points with no overlapping uncertainties and a third data point in the centre. This is why a three-way comparison is needed. The primary three sources for the weighted ANOVA and Tukey test is provided in the papers by Kutner et al. [2005]; Tukey [1949]; Montgomery [2019].

Discussion

Like the rest of the report structure, this section is split under the two different research questions investigated in this thesis, starting with the secondary goal of the report and finishing with the primary goals of the report.

5.1 Foreground Removal

A major shortfall of the foreground subtraction investigation is the lack of statistical analysis, which will be a common theme throughout this section. In some cases, this is justified, as statistical analysis in not needed if, by eye, the method clearly does not work. At the same time, this investigation is limited from a lack of characterisation of the true RM sky, including simulations to predict the distribution of corrected RMs and high-quality data to interpolate with.

This report is not meant to act as a definitive conclusion on research into foreground subtraction techniques, but to point out important considerations to make as research moves into the SKA era, and to conduct a preliminary analysis of how to tackle these predicted problems as outlined in 3.1. Section 3.1, highlights how higher-definition data will inevitably result in issues involving foreground correction for objects of a particular angular size. Thus, the need to extend beyond interpolation techniques when conducting SKA-era analysis.

The NUFFT method is one example of a method that can be assessed visually, and without the need for statistical analysis. Figure 3.2 clearly shows that even carrying out an interpolation using a NUFFT requires a large sample size to be adequate. It would not be appropriate to completely write-off NUFFTs as an interpolation and bandpass technique, as with a more complete POSSUM dataset, and future SKA RM projects, millions of RM points would be adequate to interpolate and bandpass using a NUFFT. There will simply not be enough data in the few years after this paper.

Given that the Hutschenreuter map interpolates data that is at a spatial sampling frequency of 1 sampling point per degree squared, attempting to remove objects on the scale of 1 degree should not alter the interpolation at all. However, there are several factors that prevent a perfect correlation between pre and post analyses: H-alpha inclusion providing more detailed information; more RM sources being detected by telescopes close to the Galactic midplane; and distortion effects occurring on the edges

of the cartesian version of the map. The latter two can be accounted for by performing the filtering on a reduced form of the dataset that does not include extremes in Galactic latitude. Additionally, from figure 2.3, it is clear that RMs near the Galactic midplane can become quite scattered. Even though this is true for the Hutschenreuter map, it still is a demonstration of the scatter present near the Galactic midplane.

This is the justification for the use of a Pearson's R-squared statistic for correlation, as it can determine how similar the pre and post bandpass and convolution methods, as discussed throughout section 3.5, are at preserving the broader RM sky. The expectation is that the R-squared statistic is close to unity but not necessarily exactly unity. One major downside is that there is no way to quantify the appropriate R-squared statistic that should be desired. Thus, only a high R-squared statistic is possible qualifier.

It is clear from the R-squared statistics from table 3.1 that, even with a less-exact method of determining validity, both the Crosshatch-Bandpass and Annulus-Bandpass methods are viable as an interpolation correction method. It can be pointed out that it may be unfair to compare the Annulus-Convolved method to the raw interpolation. However, it is justified in the sense that the raw interpolation has been used as the primary method in past literature, and from figure 4.3, it is demonstrably useful at removing the anisotropy produced by the ISM.

The Annulus-Bandpass method should not immediately be adopted as a method without further experimentation. The Crosshatch-Bandpass method is another viable method that should not be discounted. However, with the rippling effects shown in figure 3.3, there are improvements that can be made. The Fourier Transform of a top-hat function is inevitably going to introduce rippling. This may not be as much of the case with the Tukey or Gaussian windows, which is much more common in other signal processing analyses. The choice to reduce bandpass opacity is another option that clearly removes ripples, at the cost of dampening the intended goal of using FFT signal processing methods. Some combination of these may be useful for future research relying on RM-correction.

The interesting result provided in Anderson et al. [2024], that corrected RMs follow a t-distribution, clearly still shows with a repeated analysis on the Hutschenreuter map, and the bandpassing methods. There is still little reason for why corrected RMs take a t-distribution shape, or if this is meant to be the true distribution of RMs post ISM correction. It is rather crucial that research be conducted into what the true distribution of ISM-corrected RMs should be. It is trivial to understand why the distribution should be symmetrical and centred at zero, as extragalactic polarisation is effectively random and not biased based on sign. The Student's t-distribution is one of many different distributions satisfying these properties that are viable candidates for representing corrected RMs, it could be that the central limit theorem applies here but that there is a subpopulation of RMs that are intrinsically higher [Vanderwoude et al., 2024].

Under the assumption that it is already known why and expected that the t-distribution is a correct reflection of reality, both the original and the bandpass filters of the Hutschenreuter map align with the expected t-distribution incredibly well, as seen from table 3.1, with the parameters for the t-distribution fit being similarly identical. As mentioned in section 3.5, despite the clear visual incongruence, the important property of the t-distribution which appeared to not work with other distributions centred at zero, is the tailed prevalence. This ultimately gave such a small p-value in the Pearson's chi-squared test. Both distributions additionally are centred close to zero, with the systematic error being most likely a consequence of measurement bias or a consequence of the POSSUM dataset covering only a specific proportion of the sky. The latter can be seen in how the ISM's anisotropic distribution does not seem exactly symmetric in figure 4.3, connecting it with the amount of RMs recorded by POSSUM in a specific quadrant of the southern hemisphere, seen in figure 2.1. This is speculation, as any higher-order structure can fullfil this need.

As mentioned, the results in this report regarding foreground techniques are results which may not immediately show utility in the next year or two. However, with more accurate interpolation techniques, like the one seen in Khadir et al. [2024], the pre-SKA and SKA-era analyses of the RM sky will greatly benefit from the preliminary research direction opened by this report.

5.2   Magnetic Field Derivation

A key theme in this report is the distinction between validity and accuracy of a particular given method. As is common with first attempts at estimation, the lack of data and methodological development is apparent. This is the primary motivation for the report's focus on less on agreement and accuracy, but more on consideration of new methods and their mathematical validity. There is plenty of future work available, particularly in-terms of expanding upon the methodology of this report. The way this section of the sturctured aims to step through each component of the process in the analysis of results, from the limitations of the data from the onset, a justification of the assumptions employed in both detection and derivation, an assesment of the detection and derivation methods themselves, and lastly the implications this has on broader research.

5.2.1   Limitations of Collected Data

The current POSSUM sample size is a major hinderance to achieving the stated research objectives. With the survey in its early stages, a significant proportion of the sky is yet to be covered. This does not prevent viable analysis from being performed, however it does limit the scope of the analysis, and can affect the accuracy of the

evaluation. A large proportion of documented HVCs could not be analysed.

The use of the HI sky map from Westmeier [2018] is justified for the use of visual display and visual HVC detection, with the map being used to eliminate two HVCs for a lack of detection (HVC G282.3-38.3+117) and cartesian map distortions (HVC G298.0-81.7+127). However, the choice to use a HI map which filters out HI emission below a VLSR threshold (equivalent to a given column density threshold) can make it difficult to utilise the HI map for masking – a common method of isolating in-HVC and out-HVC RM populations. It is potentially difficult to do this even with a non-filtered HI map, as the boundary between what is and is not the HVC will always be difficult to discern. Masking would only be a first step, with the need to include RMs near but not on the HVC's HI boundary due to magnetic draping occurring outside the physical cloud itself. Any algorithm that can adapt itself to outline the specific shape of any given HVC and select the RMs within and around said outline would have to be highly complex.

The use of the Hutschenreuter map is justified given the use of interpolations in past research [Moss et al., 2013; Betti et al., 2019; Westmeier, 2018; Hill et al., 2013; Anderson et al., 2024], and the correlation analysis performed from table 3.1. It is clear as well that the Hutschenreuter map can eliminate the most important source of foreground interference – that being the ISM. This is evidenced indirectly by figure 4.3, with the elimination of the ISM's key feature being its innate anisotropy [Mao et al., 2010]. It is expected that what remains after correction is a more accurate depiction of the magnetic fields of the halo and halo objects, which is shown in the ridge-like structures in figure 4.1. However the interpolation is likely to add its own level of standard measurement error.

Removing the ridge-like structures from figure 4.1 is neccesary, as the halo itself is further random interference that is smoothed out via interpolation. This is why "background" is used in distinction to "foreground", as the halo along the line-of-sight surrounds the HVCs. It is much more difficult to remove this and must be done after or during the calculation of the line-of-sight magnetic field strengths. When determining a significant detection however, it is not of concern. This is because the HVC contribution to the RMs is superimposed onto the background RM field, meaning that a detection can still be made even if the background interferes with the HVC. The exception to this rule is if the background is so noisy or strong, that any variation of RMs created by the HVC is eliminated. While this is rare, it can potentially bias results towards HVCs with notably higher line-of-sight magnetic field strengths, an effective form of Malmquist bias. Despite this, HVCs which do not have significant contributions compared to the background should not be considered in the estimation process, as there is naturally less evidence to verify if the HVC is experiencing magnetic draping. Since most HVCs did have significant detections from the p-values in table 4.1, however, it is not of concern to the outcome of specifically this report.

Figure 4.1 and Moss et al. [2013] shows that HVCs come in a large variety of sizes, and so our selection criteria designed to ensure the RM analysis and foreground correction was tractable necessarily limits the generality of our conclusions. As RM analysis techniques mature in future, a more representative sample of HVCs can be studied.

5.2.2 Neccesity of Assumptions

As mentioned in section 4.2, four major assumptions were employed in the analysis post-HVC selection and RM correction: (1) the Galactic halo is well-mixed; (2) the weighted average of a given HVC's HI column density is approximately equivalent to its peak value; (3) HVCs are approximately spherical; and (4) the RM contribution along the line of sight is an additive. There are both reasons for the necessity of these assumptions, and clear blind spots that they present.

While there is evidence that the Galactic halo has an ionisation fraction close to unity [Grønnow et al., 2017], the main reason for this being labelled assumption is that there is very little evidence demonstrating this, if the halo is homogeneous at all. There is evidence to suggest that the gas surrounding HVCs themselves has very complex mixing patterns Heitsch et al. [2021]; Jung et al. [2023]. The ridge-like structures found in the RM background of each HVC image is evidence to suggest a lack of homogeneity, however, it could be a consequence of turbulence captured at an instantaneous moment as well. Until there is better data on the ionisation fraction surrounding HVCs and in the halo itself, the results from table 4.2 are likely to be inaccurate to within an order of magnitude. Note that by decreasing the ionisation fraction, the estimated magnetic field strengths become increasingly larger, meaning that changing the ionisation fraction would imply even larger magnetic field values, deviating even further from simulation predictions [Grønnow et al., 2018].

The second assumption exists due to limited information. That being, a difficulty in morphologically analyse HVCs given their HI profiles from Westmeier [2018], with the only other data being the peak HI column density from the Moss catalogue. HI data received by telescopes, even filtering for VLSR, is limited by Poisson noise. This naturally leads to higher HI values being weighted more in a weighted average. Equation 4.2 from Kaczmarek et al. [2017] utilises the weighted average HI column density, so it is somewhat reasonable to say that weighted HI column density is biased towards the peak value. The use of a single number is at least mathematically valid from the equation 4.2. Before applying equation 4.2, a single 'master RM' value for the HVC is constructed from the statistical aggregation of background and in-HVC RMs. This ensures that the HVC's master RM is the best representation of the RM contribution of only that HVC. The issue is that the signals from background RMs do not traverse the same HI region, and thus the respective column density would have starkly different values. If we were to convert each RM source to magnetic field

before combining them into a singular value, a completely different value would be achieved. This may introduce error in the calculation of the magnetic field as it effectively homogenises the HI column density across the HVC image. The idea is that this concern is counteracted by the fact that the background is only used as a tool to isolate the HVC's RM contribution, so that by subtracting the background RM aggregate we remove any potential influence from the background magnetic fields.

The third and fourth assumptions are more trivial in-terms of their purpose. Without the use of masking, and with the requirement of a generalised algorithm to distinguish in-HVC and out-HVC populations, the most logical first step is to pick a simple shape to act as the outline. Given that HVCs are comet-like structures [Konz et al., 2002], it is also reasonable to estimate the main bulb of HVCs as a sphere. The shortfall of this assumption is simply in how it may not correctly distinguish RM populations in more malformed HVCs, which as mentioned, are less likely to appear due to the method of HVC selection chosen. The last assumption is used very often in past research [Kaczmarek et al., 2017; Moss et al., 2013; Hill et al., 2013; Betti et al., 2019]. Thus, it is not of great concern in how it may affect the outcomes of this report, it is a fair approximation to make, given that most non-HVC RM contributions are corrected for.

5.2.3 Validity of Detection Methods

As mentioned, the Hutschenreuter map at mid-latitudes ($20° < |b| < 80°$) can have variations on one square degree. This may be problematic, as it means that the Hutschenreuter map may introduce variations in the corrected RM grid on such a scale. In fact, the ridge-like structures of the HVCs may be caused by spatial variations in interpolated data instead of it representing the true non-ISM foreground. This is why a visual comparison is made between the corrected RMs and the RMs post-average subtraction in figures 4.2 and 4.1. By taking an average of all the RMs within a neighbourhood of the HVC and subtracting it out and confirming that it looks visually like the corrected RMs, it can be demonstrated that the Hutschenreuter map is like subtraction using a constant factor i.e. the Hutschenreuter introduces no spatial variations because of interpolation. Two statistical tests in this report can further validate the qualitative analysis from figure 4.2. Given that the Crosshatch-Bandpassed, and Raw, Hutschenreuter map is correlated significantly (as seen with the R-Squared statistic in table 3.1), it means that the Hutschenreuter map is likely not creating additional spatial variations. It can also be seen that in the mid-latitudes in figure 3.6, the linear correlation is stronger. The subtraction of a constant value, that being the mean of all RMs in the field, would not alter the KS statistic or the p-value when the KS test is applied to the uncorrected RMs. In addition to this, the KS test on uncorrected RMs from table 4.1 consistently has smaller p-values in all cases, meaning that this KS test is less selective than the corrected KS test. Thus it can be quantitatively verified that

these spatial variations are not significantly affecting the results.

Note that while the KS test is more selective for corrected RMs, this implies that the Hutschenreuter map is better at correcting the foreground than no foreground correction at all, not that it introduces its own spatial interference.

Due to the current patchy coverage of POSSUM, even surrounding HVCs that overlap with the existing POSSUM dataset, there is a potential issue created from the Missing Completely at Random (MCAR) data. With this missing data, the full picture of foreground interferences or ridge-like structure variations cannot be determined and can cause the KS test to flag significant differences (detections) where detections may otherwise not be. While there are statistical methods to quantify the effect of MCAR data, such as Little's MCAR test [Li, 2013], it is far too speculative to essentially predict what the full POSSUM dataset may look like and is much more worth waiting a few more years to repeat the analysis performed by this report.

From section 4.1, there appears to be a moderate correlation between the results of the KS test and the HVC's Galactic latitude ($\sim$0.6). Fortunately, this correlation is even weaker when comparing the p-value with Galactic lattitude ($\sim$0.4). Any level of correlation implies that the KS test itself is biased towards HVCs of a particular Galactic latitude, which can damage the credibility of detections made by the KS test. Part of this could be due to a low sample size or a limited Galactic latitude range, which may artificially increase the correlation. Another possibility may be that due to RMs at mid-latitudes being less scattered and disorted, the KS test is more robust at determining a difference i.e. there is less noise in the calculated background – this case is what may introduce bias. Due to the small sample size of HVCs, whether the KS test is correlated with latitude cannot be determined, but it is important for future researchers to pay attention to this problem. There does not appear to be a correlation with other HVC properties like VLSR or VGSR.

5.2.4 Validity of Derivation Methods

To further distinguish the differences between accuracy and validity is the notion of mathematical, statistical, and experimental validity. Because a method may be valid in a mathematical abstract does not mean that it may be experimentally valid. Mathematical derivations necessarily introduce small assumptions, on top of the major four listed in the report. These assumptions may cause the method to fail when put into practice. Here, there is an expectation that all three derivation methods (Variance Subtraction, KS-EDF, Weighted Mean) have specific points of failure for any given scenario. For example, the weighted mean mathematically underestimates for situations where the HVC is face-on, as explained by the coffee-stain analogy in section 4.4. This was confirmed false by the weighted mean having a reasonable magnetic field value range in figure 4.5 – although it does appear to return small values for some HVCs indicated by the lower quartile whisker of the box plot. The KS-EDF method

overestimates due to the strongest deviation between populations likely occurring after a stationary point on the PDF, or inflexion point on the EDF, due to a delayed rise in the cumulative proportion. As a visual representation, note that the location of the x-statistic in figure 4.4 is off its nearest inflexion point by about $0.5 - 1$ radm^{-2}. All three tests in mathematically abstract and idealised situations work for most or some cases they may face. Which is why to statistically validate the results, a three-way method of analysis is required.

The use of the Weighted ANOVA test is crucial to the statistical validation of data. It allows for a three-way simultaneous comparison of the calculated values for each of the three methods while accounting for their uncertainties. If the Weighted ANOVA test returns a significance, it means that despite the apparent points of failure each method may have for a particular HVC, and the variations between each of the three methods, in general, the three methods agree with each other to some degree. Here, there is a weak agreement between each of the three methods – resulting in a 2-sigma confidence. This not as strong as a result as one may desire, but it is a starting point that demonstrates all three methods are headed in the right direction.

The use of the Tukey test (as seen in table 4.3) is meant to compare each method with each other [Tukey, 1949; Montgomery, 2019]. This two-way comparison can provide greater insight into which methods are more likely to agree or disagree with each other. As from section 4.5, it is quite apparent that the KS-EDF method is the worst performing of the three methods, which can be seen both visually and numerically. When comparing the KS-EDF method against the weighted mean, a 95% confidence of statistically significant difference is obtained – which is particularly problematic given that the weighted mean is sanctioned by research [Betti et al., 2019; Hill et al., 2013]. From this, it is reasonable to conclude that the KS-EDF method is the odd one out of the three and should be disregarded in future research. Comparing the weighted mean and variance subtraction using the reduced chi-squared statistic produced a very well-aligned goodness of fit (i.e. close to unity).

Despite the statistical confirmation of validity, there is ultimately no way to determine the experimental validity of each of these three methods without modelling. This is a recommended direction for cementing the results of the report. As expected, from table 4.2 the uncertainties are relatively large. There is no decent way at visually representing this statement due to how cluttered any given graph would be. The large uncertainties are expected. Certainly, for both variance subtraction and weighted mean, the calculation of uncertainties are mathematically justified. It was more difficult to obtain KS-EDF uncertainties, leading to a potential over-estimation of error. This only further supports the conclusion that the KS-EDF method is disfavourable.

For all three methods, some of the uncertainties in table 4.2 imply a nonexistent magnetic field within one sigma. It is important to seperate the KS test from the estimation techniques. As mentioned in section 4.5.1, if the estimation produces such large uncertainies, it does not imply a lack of detection - instead it implies that the

evaluation method is imprecise - something anticipated by the assumptions laid out in 4.2. All three methods are non-physical and not designed to test for the prescence of signature unlike the KS test. At the same time, it has been highlighted that each method can have multiple points of faliure like as discussed with the weighted mean in section 4.4, where by some consequence of morphology and orientation, the evaluation returns zero despite there clearly being a unique signature. This is the primary factor that influences uncertainties to be so large, as without a paring complex morphological analysis, a precise estimate of value is unacheivable, despite the clear marking of a signature from a simple comparison.

5.2.5 Implications of the Results

The methodologies proposed in chapter 4.4 play a role in how researchers will estimate the effect of magnetic draping, with the clear requirement of more techniques or 'angles of attack' to solving the problem of calculation for an arbitrary HVC, of arbitrary orientation, size, shape, and angular size. Effectively the goal of developing a generalised algorithm as discussed in section 1.5 is necessary to allow for astronomers to mass-estimate magnetic draping. An important caveat being that the four major assumptions being reduced in their contribution to systematic or random errors.

The implications of the magnetic draping hypothesis have significant ramifications on the future of galactic archaeological research. It would necessarily mean that HVCs are protected by magnetic fields, which helps to confirm a lot of *qualitative* conclusions of past research done on modelling and predictions of HVC survivability (Grønnow et al. simulations). It additionally aligns with other observations of HVCs, specifically the Smith Cloud [Betti et al., 2019; Hill et al., 2013]. While it confirms the efforts made by past research, it can help bring the field one step closer to understanding the origins of pristine gas for star-forming galaxies, with a proven method for how galaxies can obtain said gas. A small proportion of HVCs that did not have significant magnetic field detections – specifically HVCs G089.0-64.7-311 and G248.9+36.8+181. If this were not caused by methodological error, a re-examination of both HVCs is required.

While the conclusions point towards magnetic draping to three sigma confidence, the order of magnitude higher magnetic field values is of notable interest. This conflicts with precious simulational data such as in the Grønnow et al. simulations. It also implies that the Smith Cloud is less exceptional of a HVC than initially beleived. This order of magnitude increase should result in other consequences that should be measureable - most notably both Rayleigh-Taylor instabilites in the HVC gas and a significant slowing effect of HVCs due to magnetic pressure. The former of these could explain the complex mixing around HVCs [Bron, Emeric et al., 2021]. The outcomes of the methods detailed in this report will not just aid research on HVCs, but on other astronomical objects, such as molecular clouds [Tahani et al., 2024].

Conclusions

Of 13 HVCs analysed in this report, a statistical detection of a magnetic field signature of 11 HVCs was found to within 99.9% confidence. Two new methods (KS-EDF, and variance subtraction) to evaluate the magnitude of magnetic fields were proposed, in addition to the use of a previously sanctioned method (weighted average). All three methods agree with each other to within 95% confidence. Despite this, the KS-EDF poses more problems for uncertainty and estimation, at least statistically. Whereas both the variance subtraction and weighted mean methods agree with each other, having a reduced chi-squared statistic of 1.088. The mean and median HVC magnetic field is on the order of magnitude of 1 μG – a factor of 10 larger than in some of the provided simulations (Grønnow et al. simulations), but reasonable in the simulations by Jung et al. [2022].

The investigation focused on a small sample size of HVCs, with a very specific Galactic latitude range - while this is neccesary for preliminary analysis, repeating the estimation but with more HVCs and more data is needed to assess the efficacy of this report's conclusion. The circular HVC assumption is an approximation that should be improved on by a more complex morphology analysis algorithim. Perhaps the use of artificial intellegence, or dimensional analysis can provide a more definitive deliniation of HVC shape. HI and H-alpha maps can be used to additionally remove the shortfalls of assuming a singular HI column density for each HVC. Further research needs to be done in the gathering of ionisation fraction data, like in Bron, Emeric et al. [2021], a more accurate estimate of ionisation fraction can help improve the reliability of the magnetic field estimates. Modelling should be conducted to validate the methods of estimation discussed in this report.

A secondary focus was on the investigation of image processing to solve anticipated issues with higher-quality SKA-era interpolated rotation measure data. It was found that a two-dimensional bandpass filter was effective at preserving the rotation measure distribution of a lower-quality interpolations, while filtering out for objects of desired spatial wavelength. It is important, however, that future investigation is done on different bandpass window shapes and opacities, to reduce rippling effects. While the use of NUFFTs were shown to be ineffective as a combined interpolation and filtering method, it may be more useful when the POSSUM dataset is in its late stages of compilation.

Bibliography

ANDERSON, C. S., McCLURE-GRIFFITHS, N. M., RUDNICK, L., GAENSLER, B. M., O'SULLIVAN, S. P., BRADBURY, S., AKAHORI, T., BAIDOO, L., BRUGGEN, M., CARRETTI, E., DUCHESNE, S., HEALD, G., JUNG, S. L., KACZMAREK, J., LEAHY, D., LOI, F., MA, Y. K., OSINGA, E., SETA, A., STUARDI, C., THOMSON, A. J. M., ECK, C. V., VERNSTROM, T., AND WEST, J., (2024). Probing the magnetised gas distribution in galaxy groups and the cosmic web with possum faraday rotation measures. *Monthly Notices of the Royal Astronomical Society*, 533(4), 4068–4080. (cited on pages 16, 27, 42, and 44)

ARIAS-CASTRO, E. AND DONOHO, D. L., (2009). Does median filtering truly preserve edges better than linear filtering? *The Annals of Statistics*, 37(3), 1172–1206. doi: 10.1214/08-AOS604. (cited on page 28)

BAGCHI, S. AND MITRA, S., (1996). The nonuniform discrete fourier transform and its applications in filter design. ii. 2-d. *IEEE Transactions on Circuits and Systems II: Analog and Digital Signal Processing*, 43(6), 434–444. doi:10.1109/82.502316. (cited on page 19)

BECK, A. M., LESCH, H., DOLAG, K., KOTARBA, H., GENG, A., AND STASYSZYN, F. A., (2012). Origin of strong magnetic fields in milky way-like galactic haloes. *Monthly Notices of the Royal Astronomical Society*, 422(3), 2152–2163. doi:10.1111/j.1365-2966. 2012.20759.x. (cited on pages vii, 3, and 14)

BETTI, S. K., HILL, A. S., MAO, S. A., GAENSLER, B. M., LOCKMAN, F. J., McCLURE-GRIFFITHS, N. M., AND BENJAMIN, R. A., (2019). Constraining the magnetic field of the smith high-velocity cloud using faraday rotation. *The Astrophysial Journal*, 871(2), 215. doi:10.3847/1538-4357/aaf886. (cited on pages 3, 4, 16, 35, 44, 46, 48, and 49)

BLAND-HAWTHORN, J. AND MALONEY, P. R., (1999). The galactic halo ionizing field and h alpha distances to hvcs. *arXiv*. doi:10.48550/arXiv.astro-ph/9812297. (cited on page 6)

BRENTJENS, M. A. AND DE BRUYN, A. G., (2005). Faraday rotation measure synthesis. *Astronomy & Astrophysics*, 441(3), 1217–1228. doi:10.1051/0004-6361:20052990. (cited on page 4)

BRON, EMERIC, ROUEFF, EVELYNE, GERIN, MARYVONNE, PETY, JÉRÔME, GRATIER, PIERRE, LE PETIT, FRANCK, GUZMAN, VIVIANA, ORKISZ, JAN H., DE SOUZA MAGALHAES, VICTOR, GAUDEL, MATHILDE, VONO, MAXIME, BARDEAU, SÉBASTIEN, CHAINAIS, PIERRE, GOICOECHEA, JAVIER R., HUGHES, ANNIE, KAINULAINEN, JOUNI, LANGUIGNON, DAVID, LE BOURLOT, JACQUES, LEVRIER, FRANÇOIS, LISZT, HARVEY, ÖBERG, KARIN, PERETTO, NICOLAS, ROUEFF, ANTOINE, AND SIEVERS, ALBRECHT, (2021). Tracers of the ionization fraction in dense and translucent gas - i. automated exploitation of massive astrochemical model grids. *Astronomy & Astrophysics*, 645, A28. doi:10.1051/0004-6361/202038040. (cited on pages 49 and 50)

DURSI, L. J. AND PFROMMER, C., (2008). Draping of cluster magnetic fields over bullets and bubbles—morphology and dynamic effects. *The Astrophysial Journal*, 677(2), 993. doi:10.1086/529371. (cited on page 3)

FERRIÈRE, K. M., (2001). The interstellar environment of our galaxy. *Reviews of Modern Physics*, 73(4), 1031–1066. doi:10.1103/RevModPhys.73.1031. (cited on page 5)

FINKBEINER, D. P., (2003). A full-sky hα template for microwave foreground prediction. *The Astrophysial Journal*, 146(2), 407. doi:10.1086/374411. (cited on pages 3, 6, and 13)

GAENSLER, B. M., HEALD, G. H., McCLURE-GRIFFITHS, N. M., ANDERSON, C. S., ECK, C. L. V., WEST, J. L., THOMSON, A. J. M., LEAHY, J. P., RUDNICK, L., MA, Y. K., AKAHORI, T., GÜRKAN, G., LANDECKER, T. L., MAO, S. A., O'SULLIVAN, S. P., RAJA, W., SUN, X., VERNSTROM, T., BAIDOO, L., CARRETTI, E., TAYLOR, A. R., WILLIS, A., OSINGA, E., LIVINGSTON, J. D., AN, T., BRACCO, A., BRÜGGEN, M., ESWARAIAH, C., ENSSLIN, T., UPASANA, G., IDEGUCHI, S., JUNG, S. L., KACZMAREK, J. F., KOTHES, R., LAZAREVIĆ, S., LEAHY, D., LOI, F., PANDHI, A., PRICE, J. M., SHEN, A. X., SETA, A., SOBEY, C., STUARDI, C., AND VELOVIĆ, V., (2024). The polarisation sky survey of the universe's magnetism (possum). i. science goals and survey description. In preperation. (cited on pages 3, 6, and 11)

GAENSLER, B. M., LANDECKER, T. L., AND TAYLOR, A. R., (2010). Survey science with askap: Polarisation sky survey of the universes's magnetism (possum). In *Bulletin of the American Astronomical Society*. (cited on pages 3 and 11)

GREENGARD, L. AND LEE, J.-Y., (2004). Accelerating the nonuniform fast fourier transform. *Society for Industrial and Applied Mathematics Reviews*, 46(3), 443–454. doi:10.1137/S003614450343200X. https://doi.org/10.1137/S003614450343200X. (cited on page 19)

GRØNNOW, A., TEPPER-GARCÍA, T., AND BLAND-HAWTHORN, J., (2018). Magnetic fields in the galactic halo restrict fountain-driven recycling and accretion. *The Astrophysial Journal*, 865(1), 64. doi:10.3847/1538-4357/aada0e. (cited on pages 3, 6, and 45)

GRØNNOW, A., TEPPER-GARCÍA, T., BLAND-HAWTHORN, J., AND FRATERNALI, F., (2022). The role of the halo magnetic field on accretion through high-velocity clouds. *Monthly Notices of the Royal Astronomical Society*, 509(4), 5756–5770. doi:10.1093/mnras/stab3452. (cited on pages 2 and 3)

GRØNNOW, A., TEPPER-GARCÍA, T., BLAND-HAWTHORN, J., AND MCCLURE-GRIFFITHS, N. M., (2017). Magnetized high velocity clouds in the galactic halo: A new distance constraint. *The Astrophysial Journal*, 845(1), 69. doi:10.3847/1538-4357/aa7ed2. (cited on pages ix, 1, 2, 3, 4, 8, 32, 33, 38, 39, 45, 49, and 50)

HAN, J. L. AND QIAO, G. J., (1994). The magnetic field in the disk of our galaxy. *Astronomy & Astrophysics*, 288, 759–772. https://ui.adsabs.harvard.edu/abs/1994AnA...288..759H. (cited on page 3)

HAYAKAWA, T. AND FUKUI, Y., (2024). Dust-to-neutral gas ratio of the intermediate- and high-velocity h i clouds derived based on the sub-mm dust emission for the whole sky. *Monthly Notices of the Royal Astronomical Society*, 529(1), 1–31. doi:10.1093/mnras/stae302. (cited on page 6)

HEITSCH, F., MARCHAL, A., MIVILLE-DESCHÊNES, M.-A., SHULL, J. M., AND FOX, A. J., (2021). Mass, morphing, metallicities: the evolution of infalling high velocity clouds. *Monthly Notices of the Royal Astronomical Society*, 509(3), 4515–4531. doi:10.1093/mnras/stab3266. https://doi.org/10.1093/mnras/stab3266. (cited on pages 33, 34, and 45)

HEITSCH, F. AND PUTMAN, M. E., (2009). The fate of high-velocity clouds: Warm or cold cosmic rain? *The Astrophysial Journal*, 698(2), 1485. doi:10.1088/0004-637X/698/2/1485. (cited on page 2)

HILL, A. S., HAFFNER, L. M., AND REYNOLDS, R. J., (2009). Ionized gas in the smith cloud. *The Astrophysial Journal*, 703(2), 1832. doi:10.1088/0004-637X/703/2/1832. (cited on pages 1, 6, and 8)

HILL, A. S., MAO, S. A., BENJAMIN, R. A., LOCKMAN, F. J., AND MCCLURE-GRIFFITHS, N. M., (2013). Magnetized gas in the smith high velocity cloud. *The Astrophysial Journal*, 777(1), 55. doi:10.1088/0004-637X/777/1/55. (cited on pages 3, 4, 8, 10, 16, 33, 35, 44, 46, 48, and 49)

HOTAN, A. W., BUNTON, J. D., CHIPPENDALE, A. P., WHITING, M., TUTHILL, J., MOSS, V. A., MCCONNELL, D., AMY, S. W., HUYNH, M. T., ALLISON, J. R., AND ET AL., (2021). Australian square kilometre array pathfinder: I. system description. *Publications of the Astronomical Society of Australia*, 38, e009. doi:10.1017/pasa.2021.1. (cited on page 11)

Huang, T., Yang, G., Tang, and G., (1979). A fast two-dimensional median filtering algorithm. *IEEE Transactions on Acoustics, Speech, and Signal Processing*, 27(1), 13–18. doi:10.1109/TASSP.1979.1163188. (cited on page 28)

Hutschenreuter, S., Anderson, C. S., Betti, S., Bower, G. C., Brown, J.-A., Brüggen, M., Carretti, E., Clarke, T., Clegg, A., Costa, A., Croft, S., Eck, C. V., Gaensler, B. M., de Gasperin, F., Haverkorn, M., Heald, G., Hull, C. L. H., *, Inoue, M., Johnston-Hollitt, M., Kaczmarek, J., Law, C., Ma, Y. K., MacMahon, D., Mao, S. A., Riseley, C., Roy, S., Shanahan, R., Shimwell, T., Stil, J., Sobey, C., O'Sullivan, S. P., Tasse, C., Vacca, V., Vernstrom, T., Williams, P. K. G., Wright, M., and Ensslin, T. A., (2022). The galactic faraday rotation sky 2020. *Astronomy & Astrophysics*, 657(A43). doi:10.1051/0004-6361/202140486. (cited on pages 3, 11, 12, 13, and 16)

Hutschenreuter, S. and Ensslin, T. A., (2020). The galactic faraday depth sky revisited. *Astronomy & Astrophysics*, 633(A150). doi:10.1051/0004-6361/201935479. (cited on pages 3, 11, 12, 13, and 16)

Jones, T. W., Ryu, D., and and, I. L. T., (1996). The magnetohydrodynamics of supersonic gas clouds: Mhd cosmic bullets and wind-swept clumps. *The Astrophysial Journal*, 473(1), 365. doi:10.1086/178151. (cited on pages 2 and 3)

Jung, S. L., Grønnow, A., and McClure-Griffiths, N. M., (2022). Magnetic field draping around clumpy high-velocity clouds in galactic halo. *Monthly Notices of the Royal Astronomical Society*, 522(3), 4161–4180. doi:10.1093/mnras/stad1236. (cited on pages 3, 4, and 50)

Jung, S. L., McClure-Griffiths, N. M., and Hill, A. S., (2021). Distant probes of rotation measure structure: where is the faraday rotation towards the magellanic leading arm? *Monthly Notices of the Royal Astronomical Society*, 508(3), 3921–3935. doi:10.1093/mnras/stab2773. (cited on page 16)

Jung, S. L., McClure-Griffiths, N. M., Pakmor, R., Ma, Y. K., Hill, A. S., Eck, C. L. V., and Anderson, C. S., (2023). Sampling the faraday rotation sky of tng50: Imprint of the magnetised circumgalactic medium around milky way-like galaxies. *Monthly Notices of the Royal Astronomical Society*, 526(1), 836–853. doi:10.1093/mnras/stad2811. (cited on pages 3 and 45)

Kaczmarek, J. F., Purcell, C. R., Gaensler, B. M., McClure-Griffiths, N. M., and Stevens, J., (2017). Detection of a coherent magnetic field in the magellanic bridge through faraday rotation. *Monthly Notices of the Royal Astronomical Society*, 467(2), 1776–1794. doi:10.1093/mnras/stx206. (cited on pages 1, 4, 33, 34, 45, and 46)

KAWAGUCHI, I., (1952). On the excitation and ionization temperature of the hydrogen in the chromosphere. *Publications of the Astronomical Society of Japan*, 4, 131. (cited on page 6)

KHADIR, A., PANDHI, A., HUTSCHENREUTER, S., GAENSLER, B. M., VANDERWOUDE, S., WEST, J. L., AND O'SULLIVAN, S. P., (2024). Choosing interpolation techniques for reconstructing galactic faraday rotation. Submitted to ApJ. (cited on pages 12, 16, and 43)

KONZ, C., BRÜNS, C., AND BIRK, G. T., (2002). Dynamical evolution of high velocity clouds in the intergalactic medium. *Astronomy & Astrophysics*, 391(2), 713–723. doi: 10.1051/0004-6361:20020863. (cited on pages vii, 2, 3, and 46)

KUTNER, M. H., NACHTSHEIM, C. J., NETER, J., AND LI, W., (2005). *Applied Linear Statistical Models*. McGraw-Hill/Irwin, 5th edition. (cited on page 40)

LI, C., (2013). Little's test of missing completely at random. *The Stata Journal*, 13(4), 795–809. doi:10.1177/1536867X1301300407. (cited on page 47)

LOCKMAN, F. J., (2008). *High-Velocity Clouds Merging with the Milky Way*, chap. 53, 239–242. Springer. ISBN 978-1-4020-6932-1. (cited on page 8)

LOCKMAN, F. J., BENJAMIN, R. A., HEROUX, A. J., AND LANGSTON, G. I., (2008). The smith cloud: A high-velocity cloud colliding with the milky way. *The Astrophysial Journal*, 679(1), L21. doi:10.1086/588838. (cited on pages vii, 1, 8, and 9)

LOI, F., MURGIA, M., GOVONI, F., VACCA, V., PRANDONI, I., BONAFEDE, A., AND FERETTI, L., (2019). Simulations of the polarized radio sky and predictions on the confusion limit in polarization for future radio surveys. *Monthly Notices of the Royal Astronomical Society*, 485(4), 5285–5293. doi:10.1093/mnras/stz350. https://doi.org/10.1093/mnras/stz350. (cited on pages vii and 5)

LUCCHINI, S., HAN, J. J., HERNQUIST, L., AND CONROY, C., (2024). On the origin of high velocity clouds in the galaxy. Accepted by ApJ. (cited on page 2)

MACQUART, J.-P., EKERS, R. D., FEAIN, I., AND JOHNSTON-HOLLITT, M., (2012). On the reliability of polarization estimation using rotation measure synthesis. *The Astrophysical Journal*, 750(2), 139. doi:10.1088/0004-637X/750/2/139. https://dx.doi.org/10.1088/0004-637X/750/2/139. (cited on pages vii, 5, and 7)

MADSEN, G. J., REYNOLDS, R. J., AND HAFFNER, L. M., (2006). A multiwavelength optical emission line survey of warm ionized gas in the galaxy. *The Astrophysial Journal*, 652(1), 401. doi:10.1086/508441. (cited on pages 6 and 8)

Mao, S. A., Gaensler, B. M., Haverkorn, M., Zweibel, E. G., Madsen, G. J., McClure-Griffiths, N. M., Shukurov, A., and Kronberg, P. P., (2010). A survey of extragalactic faraday rotation at high galactic latitude: The vertical magnetic field of the milky way toward the galactic poles. *The Astrophysial Journal*, 714(2), 1170. doi:10.1088/0004-637X/714/2/1170. (cited on pages 3, 4, 5, 34, and 44)

McClure-Griffiths, N. M., Madsen, G. J., Gaensler, B. M., McConnell, D., and Schnitzeler, D. H. F. M., (2010). Measurement of a magnetic field in a leading arm high-velocity cloud. *The Astrophysial Journal*, 725(1), 275. doi:10.1088/0004-637X/725/1/275. (cited on pages 1 and 16)

Montgomery, D. C., (2019). *Design and Analysis of Experiments*. Wiley, 10th edition. (cited on pages 40 and 48)

Moss, V. A., McClure-Griffiths, N. M., Murphy, T., Pisano, D. J., Kummerfeld, J. K., and Curran, J. R., (2013). High-velocity clouds in the galactic all sky survey. i. catalog. *The Astrophysial Journal*, 209(1), 12. doi:10.1088/0067-0049/209/1/12. (cited on pages x, 1, 3, 13, 16, 33, 44, 45, 46, and 59)

Pulfer, E.-M., (2019). *Different Approaches to Blurring Digital Images and Their Effect on Facial Detection*. Honour's thesis, University of Arkansas. (cited on pages viii, 18, and 23)

Putman, M., Peek, J., and Joung, M., (2012). Gaseous galaxy halos. *Annual Reviews of Astronomy & Astrophysics*, 50, 491–529. doi:10.1146/annurev-astro-081811-125612. (cited on pages 1, 2, and 6)

Schnitzeler, D. H. F. M., (2010). The latitude dependence of the rotation measures of nvss sources. *Monthly Notices of the Royal Astronomical Society: Letters*, 409(1), L99–L103. doi:10.48550/arXiv.1011.0737. (cited on pages 3, 5, 10, 14, 28, and 39)

Tahani, M., Ngo, J. M., Glover, J., Clairmont, R., Zarazua, G. M., and Plume, R., (2024). Mc-blos: Determination of the line-of-sight component of magnetic fields associated with molecular clouds. Submitted to ApJ. (cited on page 49)

Taylor, A. R., Stil, J. M., and Sunstrum, C., (2009). A rotation measure image of the sky. *The Astrophysial Journal*, 702(2), 1230. doi:10.1088/0004-637X/702/2/1230. (cited on page 3)

Tepper-García, T. and Bland-Hawthorn, J., (2017). The Smith Cloud: surviving a high-speed transit of the Galactic disc. *Monthly Notices of the Royal Astronomical Society*, 473(4), 5514–5531. doi:10.1093/mnras/stx2680. https://doi.org/10.1093/mnras/stx2680. (cited on page 8)

Tukey, J. W., (1949). Comparing individual means in the analysis of variance. *Biometrics*, 5(2), 99–114. (cited on pages 40 and 48)

Vanderwoude, S., West, J. L., Gaensler, B. M., Rudnick, L., VanEck, C. L., Thomson, A. J. M., Andernach, H., Anderson, C. S., Carretti, E., Heald, G. H., Leahy, J. P., McClure-Griffiths, N. M., O'Sullivan, S. P., Tahani, M., and Willis, A. G., (2024). Prototype faraday rotation measure catalogs from the polarisation sky survey of the universe's magnetism (possum) pilot observations. *The Astrophysial Journal*, 167(5). doi:10.3847/1538-3881/ad2fc8. (cited on pages 3, 4, and 42)

Wakker, B., (1991). High-velocity clouds. *Symposium - International Astronomical Union*, 144, 27–40. doi:10.1017/S0074180900088884. (cited on pages 1 and 6)

Wakker, B. P. and van Woerden, H., (1997). High-velocity clouds. *Annual Reviews of Astronomy & Astrophysics*, 35, 217–266. doi:10.1146/annurev.astro.35.1.217. (cited on pages 1 and 6)

Westmeier, T., (2018). A new all-sky map of galactic high-velocity clouds from the 21-cm hi4pi survey. *Monthly Notices of the Royal Astronomical Society*, 474(1), 289–299. doi:10.1093/mnras/stx2757. (cited on pages vii, 3, 6, 13, 14, 16, 44, and 45)

Appendix

A   Developed Code and Data

All developed code and data is found in a publically-available GitHub repository as shown here: https://github.com/Olivex727/hvc-magnetic-honours-programs.

B   All HVCs

The filtered Moss catalogue is as below. The table has been modified from what was originally retrieved for display and formatting purposes. The actual Moss catalogue data can be found at VisieR: https://vizier.cds.unistra.fr/viz-bin/VizieR-3?-source=J/ApJS/209/12.

C   Planck Mission Cosmic Microwave Background Images

The source for the Planck mission's CMB temperature map is available on this website: https://www.esa.int/ESA_Multimedia/Images/2013/03/Planck_CMB/.

D   PyNUFFT Python Module

The pyNUFFT Python Module, which was used in the investigation for foreground removal, has its main documentation page here: https://pynufft.readthedocs.io/en/latest/index.html

Name	RAJ200	DEJ2000	VLSR	VLSR Error	VGSR	V Dev.
G038.7-37.3-241	21 15 48.32	-11 50 19	-241.4	1.0	-131.9	-203.9
G038.8-33.2-261	21 01 03.36	-10 00 23	-261	1.0	-145.6	-223.5
G043.4-30.4-230	20 58 09.18	-05 16 07	-230.7	1.0	-100.4	-193.2
G089.0-64.7-311	23 56 11.31	-05 36 13	-311.7	1.0	-217.9	-274.2
G133.5-75.6-294	01 02 11.56	-13 00 21	-294.1	1.8	-254.6	-261.6
G248.9+36.8+181	10 08 09.38	-08 21 50	181.6	4.6	17.3	139.1
G261.5-34.5+237	05 22 03.94	-53 57 52	237	2.7	57.8	194.5
G262.4-26.2+143	06 19 11.01	-54 00 25	143.6	1.9	-52	101.1
G264.6-53.3+224	03 17 32.52	-51 33 15	224.2	2.2	93.3	186.7
G267.1-38.4+263	04 51 25.06	-58 06 39	263.9	11.5	91.9	226.4
G271.6-48.4+297	03 32 17.39	-57 45 07	297	1.1	151.1	259.5
G271.7-53.1+254	03 03 24.54	-55 14 30	254.3	2.6	122.4	216.8
G323.0+25.6+122	14 18 59.71	-33 43 42	122.2	1.3	3.1	84.7

Name	FWHM	T_b Fit	N_{HI}	N_{HI} Error	Area	dx	dy
G038.7-37.3-241	12.2	0.87	3.00E+19	1.00E+18	1.5	4.2	3.0
G038.8-33.2-261	20.7	0.94	4.00E+19	2.00E+18	2.2	4.9	3.9
G043.4-30.4-230	22.9	0.64	3.00E+19	2.00E+18	1.6	3.4	3.0
G089.0-64.7-311	18.9	0.5	2.00E+19	2.00E+18	1.4	3.4	3.1
G133.5-75.6-294	26.8	0.42	2.00E+19	3.00E+18	1.3	4.2	1.4
G248.9+36.8+181	22.4	0.13	1.00E+19	2.00E+18	1.1	2.1	1.6
G261.5-34.5+237	26.6	0.28	6.00E+18	3.00E+18	1.5	2.6	2.0
G262.4-26.2+143	19.5	0.28	1.00E+19	2.00E+18	1.6	3.1	2.6
G264.6-53.3+224	22.6	0.28	1.00E+19	2.00E+18	1.7	2.6	2.7
G267.1-38.4+263	30	0.07	9.00E+18	3.00E+18	1.9	3.0	3.0
G271.6-48.4+297	21.5	0.53	2.00E+19	2.00E+18	1.8	2.1	4.6
G271.7-53.1+254	26.4	0.28	1.00E+19	3.00E+18	1.2	2.2	1.8
G323.0+25.6+122	20.8	0.43	2.00E+19	2.00E+18	1.4	2.1	2.4

Table A: Numerical values for all 13 HVCs being analysed in the report. Retrieved from Moss et al. [2013].

E   Statistical ANOVA Tests

The R language was used to calculate all tests mentioned in 4.5.2, the file is available here: https://github.com/Olivex727/hvc-magnetic-honours-programs/blob/main/KS_confirmation/wgt_anova.R. This R-Code, in addition to the research of the Weighted ANOVA and Tukey HSD test was aided by the ANU SSN Consultancy Group. See the Acknowledgements for more.

   The specific R code output when running this file is as follows:

```
> summary(base_V2_aov)
Df Sum Sq Mean Sq F value Pr(>F)
data_new$variable.x  2   44.7  22.349   3.375 0.0388 *
Residuals           87  576.1   6.622
---
Signif. codes:  0 '***' 0.001 '**' 0.01 '*' 0.05 '.' 0.1 ' ' 1
> tukey.test
Tukey multiple comparisons of means
95% family-wise confidence level

Fit: aov(formula = data_new$Estimate ~ data_new$variable.x,
weights = data_new$prescision)

$'data_new$variable.x'
   diff        lwr          upr      p adj
Var_Sub-KS_EDF   -1.199 -2.783335  0.38533482 0.1741072
Wgt_Mean-KS_EDF  -1.675 -3.259335 -0.09066518 0.0357301
Wgt_Mean-Var_Sub -0.476 -2.060335  1.10833482 0.7544765

>
```

   A copy of this text output is available in the file: https://github.com/Olivex727/hvc-magnetic-honours-programs/blob/main/KS_confirmation/chisq.txt.